INTERNATIONAL JOURNAL FOR NUMERICAL METHODS IN FLUIDS
Int. J. Numer. Meth. Fluids 2002; **38**:811–848 (DOI: 10.1002/fld.238)

A low-dimensional spectral approach for the nonlinear overstability of purely elastic fluids

Roger E. Khayat*,†

Department of Mechanical and Materials Engineering, University of Western Ontario,
London, Ontario, N6A 5B9, Canada

SUMMARY

The conditions for the emergence and stability of finite amplitude purely elastic (non-inertial) overstability are examined for axisymmetric Taylor–Couette flow of an Oldroyd-B fluid in the narrow-gap limit. The study is a detailed account of the formulation and results published previously [Khayat, *Phys. Rev. Lett.* 1997; **78**:4918]. The flow field is obtained as a truncated Fourier representation for velocity, pressure and stress in the axial direction, and in terms of symmetric and antisymmetric Chandrasekhar functions along the radial direction. The Galerkin projection of the various modes onto the conservation and constitutive equations leads to a closed low-dimensional nonlinear dynamical system with 20° of freedom. In contrast to our previous model that was based on the simplifying rigid-free boundary conditions [Khayat, *Phys. Fluids A* 1995; **7**:2191], the present formulation incorporates the more realistic rigid–rigid boundary conditions, and is capable of capturing quantitatively the flow sequence observed in the experiment of Muller *et al.* [*J. Non-Newtonian Fluid Mech.* 1993; **46**:315] for a highly elastic (Boger) fluid under conditions of negligible inertia. Existing linear analysis results are first recovered by the present formulation, which predict the exchange of stability between the circular Couette flow and oscillatory Taylor vortex flow via a postcritical Hopf bifurcation as the Deborah number exceeds a critical value. The stability conditions of the limit cycle are determined using the method of multiple scales. The present nonlinear theory predicts, as experiment suggests, the growth of oscillation amplitude of the velocity and the emergence of higher harmonics in the power spectrum as the Deborah number increases. Good agreement is obtained between theory and experiment. Copyright © 2002 John Wiley & Sons, Ltd.

KEY WORDS: stability; elastic overstability; low-order dynamic models

1. INTRODUCTION

The existence of purely elastic overstable flow for a fluid rotating between two concentric circular cylinders has been established from linear stability analysis, but a theory has yet to be found that reproduces quantitatively the evolution of finite amplitude flow in the post-critical range observed experimentally. The purpose of the present study is to show that a

---

*Correspondence to: R. E. Khayat, Department of Mechanical and Materials Engineering, The University of Western Ontario, London, Ontario N6A 5B9, Canada.

†E-mail: rkhayat@eng.uwo.ca

Received November 2000
Revised June 2001

low-dimensional dynamical systems approach can be effectively used to predict accurately the flow of highly elastic fluids. The experiments of Muller *et al.* [1] indicate a dramatic departure in the stability and bifurcation pictures for the Taylor–Couette flow of such fluids, in comparison to Newtonian fluids. While the loss of stability of the circular Couette flow (CF) of a Newtonian fluid is inertia driven, that of a viscoelastic fluid can be of purely elastic origin.

For a Newtonian fluid, it is observed that at a sufficiently small Reynolds number, Re, there is a unique stationary CF, which is globally stable. When Re exceeds a critical value, Re_c, the stationary flow loses its stability and develops a regular cellular vortex structure in which closed ring vortices alternating in sign are wrapped round the axis of rotation. In the postcritical range of Reynolds numbers, the flow remains essentially time independent and axisymmetric. This is the well-known Taylor vortex flow (TVF) after Taylor who was the first to examine this flow regime both theoretically and experimentally [2]. At some higher Re value, the stationary cellular structure loses its stability, in turn, to another structure with a different number of vortices [3, 4]. The upper limit of the TVF regime coincides with the emergence of time-dependent flow and the breaking of axisymmetry. Simultaneously, there appears a uniformly rotating pattern, or wavy vortex flow (WVF), of tangential azimuthal traveling waves superimposed on the cellular structure of TVF [5].

For viscoelastic flows, most experiments have been carried out for polmeric solutions, which are often designated as Boger fluids [6, 7]. These are highly elastic fluids with constant (shear independent) viscosity. For such fluids, elastic normal stresses (which lead to the well-known Weissenberg rod-climbing phenomenon) prohibit the onset of steady TVF as inertia is dominated by elastic effects; instead, an oscillatory TVF sets in. Recent experiments were carried out by Muller *et al.* [1] under conditions of vanishingly small Reynolds number, and by Larson *et al.* [8] and Shaqfeh *et al.* [9] in the inertio-elastic range. The experiments clearly demonstrate the existence of a purely elastic overstable mode when the Deborah number, De, which is the ratio of the relaxation time of the fluid to a typical hydrodynamic time, reaches a critical value, De_c. A mechanism for the onset of overstability was earlier proposed for the narrow-gap [8] and the wide-gap [9] configurations.

Similarly to any flow in the transition regime, the TVF of viscoelastic fluids involves a continuous range of excited spatio-temporal scales [10]. In order to assess the effect of the motion of the arbitrarily many smaller length and time scales, one would have to resolve in detail the motion of the small scales. This issue remains unresolved since, despite the great advances in storage and speed of modern computers, it will not be possible to resolve all of the continuous ranges of scales in the transition regime. It is by now well established that low-order dynamical systems can be a viable alternative to conventional numerical methods as one strives to probe the nonlinear range of flow behavior [11, 12]. The relative simplicity of low-order dynamical systems, and the rich sequence of nonlinear flow phenomena exhibited by their solution, have been the major contributing factors to their widespread use as models for examining the onset of chaotic motion. Despite the severe degree of truncation in the formulation of these equations, some of the basic qualitative elements of the onset of vortex structures have been recovered using low-order dynamical models. Since the seminal work of Lorenz [13], low-order dynamical systems have typically been used to handle simple flow configurations [14], particularly the Rayleigh–Benard thermal convection [15–20] and Taylor–Couette flow [21–24] problems. Experimental evidence for low-order dynamics has also been demonstrated for Taylor-vortex flow [25, 26]. The validity of the low-dimensional description was also established for the Taylor–Couette flow of a Newtonian fluid [23, 24]. The solution to the full Navier–Stokes equations was obtained by implementing an exact finite-difference scheme, and an approximate approach based on the Galerkin projection method and truncated Fourier representation of the flow field. Comparison of flows based on the two methods led to good agreement. However, low-dimensional models are expected to be valid in the vicinity of the critical point(s). Higher order modes must be included if the model is expected to capture the nonlinear dynamics that arises usually far beyond criticality. This approach has mainly been devised to handle simple flow configurations. However, more recently, attempts have been made to apply low-order dynamical systems for complex geometry [27–30].

Although low-order dynamical systems have mainly been formulated for Newtonian fluids, they have only recently been attempted for non-Newtonian flows [30]. Khayat and associates implemented a low-order dynamical system approach for non-Newtonian fluids in thermal convection [31–34], rotating flow [35–37], as well as in channel flow [38]. Shear thinning flows [34, 37] were modeled using truncation levels similar to the Lorenz model [13]. In this case, nonlinearities stem from inertia and the dependence of viscosity on the rate-of-strain tensor, but the resulting three-dimensional system is similar to the Lorenz equations. It must be noted that this level of truncation is too severe to expect any meaningful physics far beyond the critical point to be captured. However, low-order models can be useful in giving a simplified version of the complex dynamics that is bound to arise when higher order modes are included. In some situations, the dynamics predicted by low-order models is qualitatively the same as that predicted by the 'exact' solution. This is what has been observed in the case of purely elastic fluid systems, such as the TVF of a Boger fluid that is presently examined.

Recent theoretical work, for axisymmetric and non-axisymmetric flows, has also been examining the linear stability of viscoelastic fluids [8, 9, 39], and nonlinear stability as well [40–42]. The reader is referred to Shaqfeh [43] for a recent review. New phenomena are constantly being attributed to fluid elasticity [44, 45]. The existence of a Hopf bifurcation at the critical Deborah number was proved from linear stability analysis in the narrow-gap limit [8] and for wide gap flows [9]. Linear stability analysis indicates that, in the absence of inertia, the base (Couette) flow loses its stability to an overstable mode as the Deborah or Weissenberg number exceeds a critical value. Unlike Newtonian fluids, which obey Newton's law of viscosity, viscoelastic fluids are not governed similarly by a universal constitutive law. The dependence of the predicted flow behavior on the particular choice of a constitutive model adds another difficulty in our attempt to interpret an already complex flow situation, particularly in the transition and turbulent regimes. Larson [46] carried out a linear stability analysis in the narrow-gap limit, using the Doi-Edwards and K-BKZ constitutive equations. Additional analysis was also carried out for fluids with a distribution of relaxation times [47]. The dependence of the critical Reynolds number, Re_c, on De for the onset of TVF was found to be generally non-monotonic, but the flow is increasingly destabilized by fluid elasticity in the higher De range [46]. Numerical solutions were also obtained for the TCF of an upper-convected Maxwell (UCM) fluid, again neglecting inertia, by Northey *et al.* [40] using the finite-element method. Although their calculations confirmed the existence of a stable Hopf bifurcation at for $De > De_c$, they encountered numerical instabilities, and the range of De values for which the solution was obtainable was extremely narrow.

In an effort to probe further the nonlinear regime, Khayat [35] examined the interplay between inertia and elasticity for finite amplitude Taylor vortex flow using a severely truncated Galerkin representation of the full set of conservation and constitutive equations. The study focused on the influence of elasticity and retardation on the stability and amplitude of the

Taylor vortices in the presence of inertia. The rigid-free boundary conditions were used; it was assumed that the fluid adheres to the inner and outer cylinders in the azimuthal direction, and slips in the axial direction. Elastic effects were assumed to be weak in comparison to those of inertia, and higher order normal stress terms were neglected. This led to a six-dimensional nonlinear system, which reduces to Kuhlmann's three-dimensional system for a Newtonian fluid [23]. The low-order model system derived in the previous study [35] could not possibly reproduce reasonably the flow sequence reported in the experiment of Muller *et al.* [1] for vanishingly low-Reynolds number. The major reason for this is the severe level of truncation in the solution representation, and the use of the rigid-free boundary conditions. The neglected higher order terms, in the normal stress, particularly $\tau_{\theta\theta}$, become important in the limit $De \gg Re$, thus restricting the model to inertia dominant flow. This term turns out to be significant in the limit of small Reynolds number. Although the previous formulation is not adequate for the investigation of the purely elastic overstability or even a flow with negligible inertia ($Re \ll De$), it was possible to establish a good qualitative agreement between the numerical results and the experimental measurements of Muller *et al.* [1].

In the present study, a judicious mode selection process is carried out to determine the type and number of the most dominant modes. Attention is focused on the TCF of a highly elastic fluid of the Boger type. The work is particularly focused on the instability of TCF of high-molecular-weight fluids, typically composed of a Newtonian solvent and a polymeric solute. A short summary of the results was communicated earlier in a letter [36]. Here a complete account of the mathematical formulation, numerical implementation and physical analyses are given. In order to make the formulation more tractable, inertia is neglected. The assumption of stress-free condition along the axial direction is also relaxed. The validity of the approximate solution is established upon comparison with existing linear stability results and experiment. A multiple-scale analysis is carried out to examine the conditions for stability of the emerging limit cycle under the influence of time relaxation, viscosity ratio, wave number and gap-to-radius ratio. The ultimate aim is to recover quantitatively the experimental measurements of Muller *et al.* [1], and predict what may happen to the flow as the Deborah number is raised beyond the range of experimental values.

The paper is organized as follows. In Section 2, the conservation and constitutive equations are derived in the narrow-gap limit for an Oldroyd-B fluid. The nonlinear dynamical system is then derived through a truncated representation of the flow field in terms of Fourier and Chandrasekhar modes. In Section 3 linear stability analysis and comparison with existing (exact) results are presented, together with a multiple scale analysis around the bifurcation point. Finite amplitude Taylor–Couette flow and comparison with experiment are presented in Section 4. Discussion and concluding remarks are covered in Section 5.

2. DERIVATION OF THE NONLINEAR DYNAMICAL SYSTEM

The derivation of the nonlinear dynamical system for a viscoelastic fluid is presented in this section. First, the conservation and constitutive equations as well as the boundary conditions are examined in the narrow-gap limit. The solution of these equations is represented in terms of an infinite number of discrete Fourier modes in the axial direction and Chandrasekhar functions in the radial direction, which, upon truncation and application of the Galerkin projection, leads to the finite dynamical system that governs the expansion coefficients.

2.1. General equations and boundary conditions

Consider an incompressible viscoelastic fluid of density ρ, relaxation time λ_1 and viscosity η. In this study, only fluids that can be reasonably represented by a single relaxation time and constant viscosity are considered. The fluid is assumed confined between two infinite and concentric cylinders of inner and outer radii R_i and R_o, respectively. The present study is limited to axisymmetric flow. The inner cylinder is taken to be rotating at an angular velocity Ω, while the outer cylinder is at rest. In cylindrical polar coordinates $(\mathbf{E}_R, \mathbf{E}_\Theta, \mathbf{E}_Z)$, the conservation of mass and linear momentum equations are, respectively, (upper-case Latin and Greek notations are used to denote dimensional variables)

$$\nabla \cdot \mathbf{U} = 0, \quad \nabla P + \nabla \cdot \Sigma = \mathbf{0} \tag{1}$$

where the inertia terms have been neglected. The assumption of negligible inertia is usually valid for polymeric flows as viscous effects tend to be dominant. Here P is the hydrostatic pressure, $\nabla = \mathbf{E}_R(\partial/\partial R) + \mathbf{E}_\Theta(\partial/R\partial\Theta) + \mathbf{E}_Z(\partial/\partial Z)$ is the gradient operator, $\mathbf{U}$ is the velocity vector (U_R, U_Θ, U_Z) and Σ is the corresponding (symmetric) deviatoric stress tensor with components $\Sigma_{RR}, \Sigma_{R\Theta} = \Sigma_{\Theta R}, \Sigma_{RZ} = \Sigma_{ZR}, \Sigma_{\Theta\Theta}, \Sigma_{\Theta Z} = \Sigma_{Z\Theta}, \Sigma_{ZZ}$. An appropriate constitutive equation is needed for Σ.

Although the stability picture is expected to be significantly influenced by the constitutive model, the present formulation will be restricted to the so-called Boger fluids, which obey the Oldroyd-B constitutive equation. The resulting flow will be compared with that observed in the experiment of Muller *et al.* [1]. Some of the properties of Boger fluids are summarized by Larson *et al.* [8], and are discussed here for completeness. The test fluid used in the experiment is a dilute solution of a flexible high-molecular-weight isobutylene in a viscous low-molecular-weight solvent (polybutene), and is well described by the three-parameter Oldroyd-B equation. The fluid is a highly elastic of constant (shear independent) viscosity. The Oldroyd-B constitutive equation thus predicts no shear thinning, and the first normal stress coefficient is constant, which is consistent with the measurements of the properties of dilute solutions [50, 51]. The Oldroyd-B equation also predicts that the second normal stress difference is zero, which is in rough agreement with rheological measurements [52]. In this case, the deviatoric stress tensor Σ consists of the sum of a Newtonian (solvent) and a polymeric contributions:

$$\Sigma = T - \eta_s \Gamma \tag{2}$$

where $\Gamma \equiv \nabla\mathbf{U} + (\nabla\mathbf{U})^t$ is the strain-rate tensor, η_s is the solvent viscosity and T is the elastic part of Σ, which satisfies the upper-convected Maxwell equation [6]:

$$\overset{\nabla}{T} \equiv \lambda_1 \left[\frac{\partial T}{\partial T} + \mathbf{U} \cdot \nabla T - (\nabla\mathbf{U})^t \cdot T - T \cdot \nabla\mathbf{U}\right] + T = -\eta_p \Gamma \tag{3}$$

where η_p is the polymeric contribution to the shear viscosity and T is the time. The following boundary conditions are imposed on the cylinder walls: (i) regardless of the nature of the two cylinders, the no-penetration condition must apply:

$$U_R(R = R_i, Z, T) = U_R(R = R_o, Z, T) = 0 \tag{4}$$

(ii) no-slip conditions in the azimuthal direction, i.e.,

$$U_\Theta(R = R_i, Z, T) = \Omega R_i, \quad U_\Theta(X = R_o, Z, T) = 0 \tag{5}$$

(iii) no-slip condition along the Z direction:

$$U_Z(R=R_i,Z,T)=0, \quad U_Z(X=R_o,Z,T)=0 \tag{6}$$

2.2. Governing equations in the narrow-gap limit

Consider now the flow between concentric cylinders in the narrow-gap limit, i.e., in the case when the radius R_i/R_o is very close to one. Suitable scales must be sought for length, time, velocity and stress. There are, in fact, several choices possible [10, 53, 54]. One obvious choice for the length scale is $d \equiv R_o - R_i$. In this case, one expects $\varepsilon = d/R_i$ to emerge as the natural perturbation parameter for the problem, no matter what the remaining scales are. The flow with a relatively small rate of rotation of the inner cylinder is of particular interest in the present work. Thus, in order to bring out the influence of elasticity through the Deborah number, De, the dimensionless variables are introduced as follows:

$$\begin{aligned} &x=\frac{R-R_i}{d}-\frac{1}{2}, \quad z=\frac{Z}{d}, \quad (u_x,u_z)=\frac{1}{R_i\Omega}(U_R,U_Z) \\ &t=\frac{R_i\Omega}{d}T, \quad u_y=\frac{U_\Theta\sqrt{\varepsilon}}{R_i\Omega}, \quad (\tau_{xx},\tau_{zz},\tau_{xz})=\frac{d}{\eta R_i\Omega}(T_{RR},T_{ZZ},T_{RZ}) \\ &p=\frac{d}{\eta R_i\Omega}P, \quad (\tau_{xy},\tau_{zy})=\frac{d\sqrt{\varepsilon}}{\eta R_i\Omega}(T_{R\Theta},T_{Z\Theta}), \quad \tau_{yy}=\frac{d}{\varepsilon\eta R_i\Omega}T_{\Theta\Theta} \end{aligned} \tag{7}$$

where, following similar arguments to those in the case of a Newtonian fluid [10], suitable scalings for the azimuthal velocity and shear stress components are used in terms of ε. The choice of scaling for $T_{\Theta\Theta}$ needs, however, some further justification. This is a somewhat trickier term to handle since it is the only stress component that completely vanishes in the case of a Newtonian fluid, and has an increasingly influential role as fluid elasticity increases. If $T_{\Theta\Theta}$ was scaled like the rest of the normal stress components in (7), then it would be the only term of order ε in the non-dimensional radial momentum equation (a comma denotes partial differentiation):

$$\tau_{xx,x}+\tau_{xz,z}+p_{,x}-\varepsilon\tau_{yy}-aRv(u_{x,xx}+u_{x,zz})=0 \tag{8a}$$

and would then have to be neglected in comparison with the rest of the stress terms on the right-hand side. Now, examining the equation governing τ_{yy}:

$$\varepsilon De(\tau_{yy,t}+u_x\tau_{yy,x}+u_z\tau_{yy,z})-2De(u_{y,x}\tau_{xy}+u_{y,z}\tau_{yz})=-\varepsilon\tau_{yy} \tag{8b}$$

with De being defined below, one immediately concludes that the term $\varepsilon\tau_{yy}$ is in fact of order De, and therefore cannot be neglected unless De itself is at most of order ε. This was indeed the assumption that was made in the earlier work [35] when the influence of weak elasticity on the onset and stability of TVF was examined.

If expressions (7) are substituted into Equations (1)–(3), one recovers the important dimensionless groups in the problem, namely the Deborah number, De, and gap-to-radius ratio, ε, which will be introduced shortly. Another parameter, Rv, is also recovered, reflecting the effect of retardation in the Oldroyd-B fluid. Typically such a fluid is composed of a Newtonian solvent and a polymeric solute, and is called Boger fluid [6]. In this case, Rv is the solvent-to-polymer viscosity ratio. One thus has

$$De = \frac{\lambda_1 R_i \Omega}{d}, \quad Rv = \frac{\eta_s}{\eta_p}, \quad \varepsilon = \frac{d}{R_i} \tag{9}$$

where η_s and η_p are recalled to be the solvent and polymer viscosity, respectively. Note that in this case $\eta = \eta_s + \eta_p$. Another related dimensionless group, which is used in the present formulation, is the polymer-to-solution viscosity ratio, a:

$$a = \frac{\eta_p}{\eta} = \frac{1}{Rv+1} \tag{10}$$

It is important to note that it is the departure flow field from the base (Couette) flow, rather than the total flow field, is of interest here. The base flow can be easily shown to be:

$$\begin{gathered} u_x^s = u_z^s = 0, \quad u_y^s = \frac{1}{2} - x, \quad \frac{dp_s}{dx} = Re(1-x)^2 - 2aDe \\ \tau_{xx}^s = \tau_{xz}^s = \tau_{zx}^s = \tau_{zz}^s = \tau_{yz}^s = \tau_{zy}^s = 0, \quad \tau_{xy}^s = \tau_{yx}^s = a, \quad \tau_{yy}^s = -2aDe \end{gathered} \tag{11}$$

The equations governing the departure from the base flow are then derived by expanding the flow field in powers of ε, and excluding terms of $O(\varepsilon)$ and higher:

$$\begin{aligned} u_i(x,z,t) &= u_i^s(x) + \varepsilon u_i(x,z,t) + O(\varepsilon) \\ p(x,z,t) &= p_s(x) + \varepsilon p(x,z,t) + O(\varepsilon) \\ \tau_{ij}(x,z,t) &= \tau_{ij}^s(x) + \varepsilon \tau_{ij}(x,z,t) + O(\varepsilon) \end{aligned} \tag{12}$$

where $i,j = x,y,z$. Thus, in the absence of inertia, the (dimensionless) continuity and momentum conservation equations for an Oldroyd-B fluid reduce to:

$$u_{x,x} + u_{z,z} = 0 \tag{13}$$

$$\tau_{xx,x} + \tau_{xz,z} + p_{,x} - \tau_{yy} - aRv(u_{x,xx} + u_{x,zz}) = 0 \tag{14}$$

$$\tau_{xy,x} + \tau_{zy,z} - aRv(u_{y,xx} + u_{y,zz}) = 0 \tag{15}$$

$$\tau_{xz,x} + \tau_{zz,z} + p_{,z} - aRv(u_{z,xx} + u_{z,zz}) = 0 \tag{16}$$

whereas the constitutive equation leads to

$$\tau_{xx,t} + u_x\tau_{xx,x} + u_z\tau_{xx,z} - 2(u_{x,x}\tau_{xx} + u_{x,z}\tau_{xz}) = -De^{-1}(\tau_{xx} + 2au_{x,x}) \tag{17}$$

$$\tau_{yy,t} + u_x\tau_{yy,x} + u_z\tau_{yy,z} - 2[(u_{y,x} - 1)\tau_{xy} + au_{y,x} + u_{y,z}\tau_{yz}] = -De^{-1}\tau_{yy} \tag{18}$$

$$\tau_{zz,t} + u_x\tau_{zz,x} + u_z\tau_{zz,z} - 2(u_{z,x}\tau_{xz} + u_{z,z}\tau_{zz}) = -De^{-1}(\tau_{zz} + 2au_{z,z}) \tag{19}$$

$$\begin{aligned}&\tau_{xy,t} + u_x\tau_{xy,x} + u_z\tau_{xy,z} - \lfloor u_{x,x}(\tau_{xy} + a) + u_{x,z}\tau_{yz} + (u_{y,x} - 1)\tau_{xx} + u_{y,z}\tau_{xz}\rfloor \\ &\quad = -De^{-1}(\tau_{xy} + au_{y,x})\end{aligned} \tag{20}$$

$$\tau_{xz,t} + u_x\tau_{xz,x} + u_z\tau_{xz,z} - (u_{z,x}\tau_{xx} + u_{x,z}\tau_{zz}) = -De^{-1}\lfloor \tau_{xz} + a(u_{x,z} + u_{z,x})\rfloor \tag{21}$$

$$\begin{aligned}&\tau_{yz,t} + u_x\tau_{yz,x} + u_z\tau_{yz,z} - \lfloor u_{z,x}(\tau_{xy} + a) + u_{z,z}\tau_{yz} + (u_{y,x} - 1)\tau_{xz} + u_{y,z}\tau_{zz}\rfloor \\ &\quad = -De^{-1}(\tau_{yz} + au_{y,z})\end{aligned} \tag{22}$$

From expressions (4)–(6), one derives the following homogeneous boundary conditions:

$$u_x(x = \pm 1/2, z, t) = u_y(x = \pm 1/2, z, t) = u_z(x = \pm 1/2, z, t) = 0 \tag{23}$$

In order for the boundary-value problem (13)–(23) to become well posed, appropriate initial conditions are needed. The choice of initial conditions in this case is not crucial since the long-term behavior is of interest.

2.3. The periodic solution in z

Consider now the general solution of Equations (13)–(22), which is assumed to be periodic along the cylinder axis. The velocity, pressure and stress fields are represented by an infinite Fourier series in the z direction, with the series coefficients depending on x and t. The Fourier modes have π/k (in units of d) as fundamental wavelength in the z direction. Each flow variable is thus written as a spectral sum of the form:

$$u_i(x,z,t) = \sum_{m=-\infty}^{\infty} u_i^m(x,t)e^{imkz}, \quad \tau_{ij}(x,z,t) = \sum_{m=-\infty}^{\infty} \tau_{ij}^m(x,t)e^{imkz} \tag{24a}$$

where

$$u_i^m(x,t) = \frac{k}{\pi}\int_0^{\pi/k} u_i(x,z,t)e^{-imkz}dz, \quad \tau_{ij}^m(x,t) = \frac{k}{\pi}\int_0^{\pi/k} \tau_{ij}(x,z,t)e^{-imkz}dz \tag{24b}$$

are the complex Fourier coefficients. Additional relations among the Fourier coefficients are obtained by examining the physical symmetry of the flow. A symmetry allowed by Equations (13)–(22), similarly to the Navier–Stokes equations [57, 56], occurs when the flow is invariant under $z \to -z$, and $u_z \to -u_z, \tau_{\alpha z} \to -\tau_{\alpha z}$ $(\alpha = x, y)$. This amounts to having invariance in flow when the Taylor–Couette apparatus is turned upside down [56]. Thus, in addition to being axisymmetric, the velocity and stress fields must satisfy the following symmetry conditions:

$$\begin{aligned}&u_\alpha(x,z,t) = u_\alpha(x,-z,t), \quad u_z(x,z,t) = -u_z(x,-z,t), \quad p(x,z,t) = p(x,-z,t) \\ &\tau_{ii}(x,z,t) = \tau_{ii}(x,-z,t), \quad \tau_{xy}(x,z,t) = \tau_{xy}(x,-z,t), \quad \tau_{\alpha z}(x,z,t) = -\tau_{\alpha z}(x,-z,t)\end{aligned} \tag{25}$$

where $i = x, y, z$ and $\alpha = x, y$. It is not difficult to see that this symmetry is preserved under the nonlinear multiplication in both the convective and upper-convective terms of Equations (13)–(22). The symmetry leads to the following simplification:

$$Im[u_\alpha^m(x,t)] = Re[u_z^m(x,t)] = Im[p_m(x,t)] = 0 \tag{26a}$$

for the velocity and pressure Fourier coefficients, and

$$Im[\tau_{ii}^m(x,t)] = Im[\tau_{xy}(x,z,t)] = Re[\tau_{\alpha z}^m(x,t)] = 0 \tag{26b}$$

for the stress coefficients. Thus, the expressions for the flow variables reduce to

$$u_x(x,z,t) = \sum_{m=0}^{\infty} u_x^m(x,t)\cos(mkz) \tag{27}$$

$$u_y(x,z,t) = \sum_{m=0}^{\infty} u_y^m(x,t)\cos(mkz) \tag{28}$$

$$u_z(x,z,t) = \sum_{m=0}^{\infty} u_z^m(x,t)\sin(mkz) \tag{29}$$

$$p(x,z,t) = \sum_{m=0}^{\infty} p^m(x,t)\cos(mkz) \tag{30}$$

$$\tau_{ii}(x,z,t) = \sum_{m=0}^{\infty} \tau_{ii}^m(x,t)\cos(mkz), \quad (i = x, y, z, \text{ no sum}) \tag{31}$$

$$\tau_{xy}(x,z,t) = \sum_{m=0}^{\infty} \tau_{xy}^m(x,t)\cos(mkz) \tag{32}$$

$$\tau_{\alpha z}(x,z,t) = \sum_{m=0}^{\infty} \tau_{\alpha z}^m(x,t)\sin(mkz), \quad (\alpha = x, y) \tag{33}$$

The Galerkin projection method is now applied. The method consists of multiplying Equations (13)–(22) by the corresponding modes above and integrating with respect to z from 0 to π/k. An infinite set of coupled partial differential equations is obtained, which govern the expansion coefficients. If Equations (13)–(22) were linear, the various modes involved would have separated in a manner similar to the case of a Newtonian fluid [59], and the first-order z-dependent terms would have to be examined. In the present nonlinear context, the zeroth-order terms are also retained in order to ensure that part of the nonlinear upper-convective terms in the constitutive equations, do not vanish in the projection process. Previously [35], all the zeroth-order coefficients τ_{ij}^0, except τ_{xy}^0, were neglected. This approximation was reasonably justified since the roles of both inertia and elasticity were examined. In the present study, however, the instability of highly elastic fluids is of concern, and a higher number of modes in shear and normal stresses must be retained. The elimination of the z dependence is detailed in Appendix A. After truncation, the resulting equations that govern the (x,t) dependent coefficients are given through the system of Equations (A1)–(A16). The solution of this system will be sought next subject to boundary conditions (A17).

2.4. *The nonlinear dynamical system*

The most crucial step in the problem formulation is seeking an orthogonal representation in x for the solution of Equations (A1)–(A16) and imposing a suitable level of truncation in order to obtain the final nonlinear dynamical system. A judicious selection process must then be applied for the choice of the various modes in order to ensure the physical and mathematical coherence of the final model. Not only does the approximate flow solution have to satisfy the imposed boundary conditions at the inner and outer cylinders, it must also reduce, in the limit of small departure from the base flow, to the corresponding solution for linear viscoelastic flow with negligible inertia. In this case, the equations reduce to those of [8] in the narrow-gap limit.

If the nonlinear terms are neglected in Equations (A1)–(A16), all the zeroth-order coefficients $u_i^0(x,t)$, $p^0(x,t)$ and $\tau_{ij}^0(x,t)$ become decoupled from the remaining variables, and decay to zero with uninteresting transients. For linear stability analysis, one sets $u_x^1(x,t)=U(x)e^{-i\omega t}$, etc., where ω is generally complex, with ω_{r} and ω_i being the real and imaginary parts, respectively. In this case, the stress components are explicitly expressed in terms of the velocity and velocity gradient through Equations (A1)–(A16). Upon elimination of the pressure from Equations (A3) and (A6), and the z velocity component from Equation (A2), the following fourth-order equation for $U(x)$ is obtained:

$$(U''-k^2U)''+\Lambda k^3U'=0 \tag{34}$$

where similar notations to those of Larson *et al.* [8] are adopted (note that a prime denotes differentiation with respect to x). In this case, the eigenvalue, Λ, of the problem is given by:

$$\Lambda=\frac{\varepsilon De^2\bar{c}}{k} \quad \text{where } \bar{c}\equiv\frac{2D^2(1+2D)(Rv+D)-2D^3(1+D)}{(Rv+D)^2} \tag{35}$$

Here $D\equiv 1/(1-i\omega De)$. The boundary conditions at the inner and outer cylinders become:

$$U(\pm 1/2)=U'(\pm 1/2)=0 \tag{36}$$

The solution of the eigenvalue problem (34) and (36) is obtained using the direct method. Similarly to Larson *et al.* [8], the solution may be written as:

$$U(x)=\sum_{i=1}^{4}A_ie^{\lambda_i x} \tag{37}$$

where the λ_i are the distinct roots of the characteristic equation corresponding to (34). Since solution (37) must also satisfy the homogeneous boundary conditions (36), there results the following system of equations for the coefficients A_i:

$$\sum_{i=1}^{4}A_i=\sum_{i=1}^{4}A_i\lambda_i=\sum_{i=1}^{4}A_ie^{\lambda_i}=\sum_{i=1}^{4}A_i\lambda_ie^{\lambda_i}=0 \tag{38}$$

The system (38) admits a nontrivial solution if the corresponding determinant is zero. The eigenvalues are determined using an iteration scheme on the initial guesses and the secant method until the determinant is less than an imposed small tolerance [8]. The eigenvalues Λ obtained using this method are found to be all imaginary leading to the same dispersion relation as that of Larson *et al.* [8]. Thus, upon setting $\omega_i = 0$ for the neutral curve in the (De, k) plane, one obtains an expression derived from the fact that the real part of Λ is always zero and gives the value of ω_r in terms of the real root(s) of the following equation:

$$Rv^3\chi^3 + Rv(7Rv^2 + Rv - 1)\chi^2 + (3Rv^3 + 2Rv^2 + 2Rv + 1)\chi$$
$$-(3Rv^3 + 7Rv^2 + 5Rv + 1) = 0 \tag{39}$$

where $\chi = (\omega_r De)^2$. Note that, in the case of a Maxwell fluid, the solution of Equation (37) reduces to $\chi = \pm 1$. This critical value, for the onset of linear overstability, and the rest of the values on the neutral stability curve, should serve as limit values. By limit values it is meant those values predicted by the nonlinear theory in the limit of small departure from the base flow, where only an approximate solution can be found.

An approximate solution to the linear problem (34)–(36) is now sought, and then compared with the exact solution from the direct method. The following truncated representation for $U(x)$ is chosen in terms of a symmetric and an antisymmetric modes:

$$U(x) = U_1\Phi_1(x) + U_2\Phi_2(x) \tag{40}$$

where $\Phi_1(x)$ and $\Phi_2(x)$ are Chandrasekhar functions [57], which are given explicitly in Appendix B.

Other orthogonal functions could also have been used [58, 59]. Upon projection of Equation (34) on each of the two modes above, and for a non-trivial solution, the following characteristic equation for Λ is obtained:

$$k^6\lambda\mu C_3C_7\Lambda^2 - (k^4 + \lambda^4 - 2k^2\lambda^2C_1)(k^4 + \lambda^4 - 2k^2\mu^2C_6) = 0 \tag{41}$$

where $\lambda, \mu, C_1, C_3, C_6$ and C_7 are constants defined in Appendix C. It is found that, for a UCM fluid ($Rv = 0$), the approximate minimum value of the Deborah number and corresponding wave number for the onset of the most unstable (overstable) mode are $\sqrt{\varepsilon}De_{\min} = 6.25$ and $k_{\min} = 5.95$, respectively, compared to the exact values 5.92 and 6.7 based on the direct method (see also Larson *et al.* [8]).

The exact solution (37), when compared with Equation (40), gives an estimate of the magnitude of the error resulting from the truncation in solution (40). It is expected that the error remains of the same order of magnitude, for small flow departure, when such a truncation is also adopted for the solution of the full nonlinear Equations (A1)–(A16). Comparison with experiment for the postcritical finite amplitude TCF will be carried out to monitor the accuracy of the solution and the effect of truncation. The neutral stability curves, based on the approximate solution (40) are shown in Figure 1 for various values of the viscosity ratio, *Rv*. The figure also includes an inset showing the exact neutral curves (which are essentially the same as those reported by Larson *et al.* [8]). It is generally clear from the figure that the two sets of curves, for all viscosity ratios, exhibit similar behavior. At small wave number, the critical Deborah number when overstability sets in decreases sharply with k, reaches a minimum at $k = k_{\min}$, and increases again for $k > k_{\min}$. All curves indicate a general flattening around $k_{\min}$, confirming the experimentally observed wide range of wave numbers at which

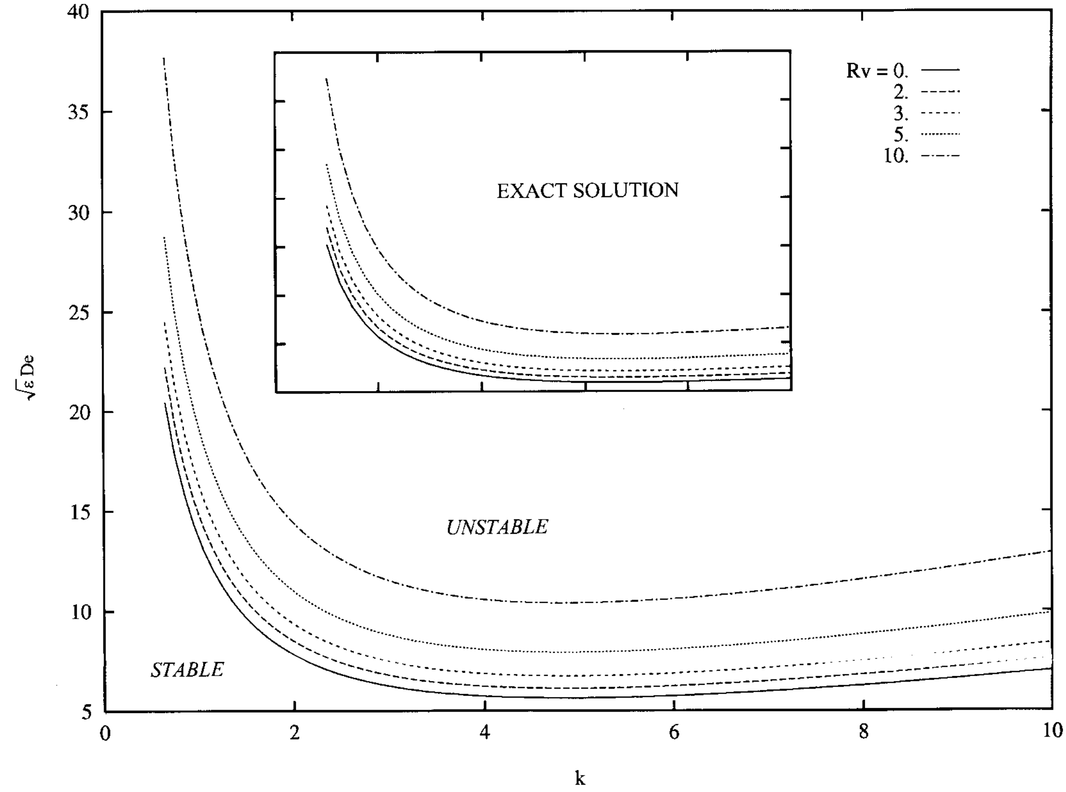

Figure 1. Marginal stability curves for the onset of purely elastic oscillatory TVF. Comparison between approximate and exact (inset) solution.

overstability sets in [7, 60, 61]. The figure indicates a close quantitative agreement between the exact solution (37) and approximate solution (40) for $k < k_{\min}$. Thus, high frequency (along the cylinder axis) perturbations tend to require a smaller number of orthogonal modes in the solution representation for $U(x)$. The exact solution tends to show a more pronounced flattening of all the curves.

On the basis of the above analysis and results, one now proceeds and imposes the same type and number of orthogonal modes that may adequately describe the nonlinear representation for Equations (A1)–(A16). It is first observed that, if only one fundamental eigenmode is kept in expression (40), only the trivial solution to problem (34) and (36) is obtained. This corresponds exactly to the level of approximation adopted in the previous work [35], where only flows with dominant inertia ($Re \gg De$) could be treated. The general solution to Equations (A2)–(A16) must then be chosen so that (1) linear behavior is reasonably recovered for small deviation from the base flow, and (2) boundary conditions (A17) are satisfied. The elimination of the x dependence is achieved by expanding the solution of Equations (A1)–(A16) in terms of the Chandrasekhar functions and their derivatives. The expansion as well as the resultant dynamical system are detailed in Appendix B.

3. EXISTENCE AND STABILITY OF PURELY ELASTIC OSCILLATORY TAYLOR–COUETTE FLOW

Although the existence of purely elastic overstable TVF is now well established from linear stability analysis [8], the conditions for its stability are yet to be addressed. For completeness, the existence of a Hopf bifurcation as the Deborah number reaches a critical value is first proven through linear stability analysis of system (B8), and then the method of multiple scales is used to examine the stability of the limit cycle near the bifurcation fixed point.

3.1. Linear stability analysis

Consider the small departure from the basic Couette flow. System (B8) is linearized around the origin by assuming the velocity and stress coefficients to take the form:

$$u_i^{ab}(t) = \bar{u}_i^{ab} e^{-i\omega t}; \quad \tau_{ij}^{ab}(t) = \bar{\tau}_{ij}^{ab} e^{-i\omega t} \tag{42}$$

where $i, j = x, y, z$ and $a, b = 0, 1, 2$. Note that barred variables are constants and $\omega = \omega_{\mathrm{r}} + i\omega_i$ is generally complex. The resulting characteristic equation is derived in Appendix D, which, in analogy to Equation (41), is cast as

$$k^6 \lambda \mu C_3 C_7 \hat{\Lambda}^2 - (k^4 + \lambda^4 - 2k^2\lambda^2 C_1)(k^4 + \lambda^4 - 2k^2\mu^2 C_6) = 0 \tag{43}$$

where, similarly to Equation (35), one lets

$$\hat{\Lambda} = \frac{\varepsilon De^2 \hat{c}}{k}, \quad \hat{c} \equiv \frac{2D^2(1+2D)(Rv+D) - 2D^3(1+D)}{(Rv+D)\sqrt{\left[Rv + \dfrac{D\tau_1^2}{k^4+\lambda^4-2C_1\lambda^2k^2}\right]\left[Rv + \dfrac{D\tau_2^2}{k^4+\mu^4-2C_6\mu^2k^2}\right]}} \tag{44}$$

In fact, Equation (43) is more complicated than Equation (41), and is therefore less amenable to algebraic manipulations except for a Maxwell fluid ($Rv = 0$). Thus, an equation similar to Equation (35) is difficult to obtain. The frequency of oscillation (or, more precisely, $\omega_{\mathrm{r}} De$), corresponding to a marginal curve (for given Rv), is obtained by setting $Re(\hat{c}) = 0$ and $\omega_i = 0$. The resulting nonlinear algebraic equation appears to have only one real root, which is then used to obtain the critical value for the Deborah number that satisfies:

$$\sqrt{\varepsilon} De = \frac{1}{k\sqrt{\mathrm{Im}(\hat{c})}} \left[\frac{(k^4 + \lambda^4 - 2k^2\lambda^2 C_1)(k^4 + \lambda^4 - 2k^2\mu^2 C_6)}{\lambda\mu C_3 C_7}\right]^{1/4} \tag{45}$$

Figure 2 displays the marginal curves based on Equation (45), which are compared to those based on Equation (41). The former curves are seen to lead generally to a slightly lower critical Deborah number (for a given wave number). Agreement is better as Rv increases or as k increases. Indeed, in the limit of infinite wave number Equations (41) and (43) lead to identical results since $\lim_{k\to\infty}(\hat{c} - \bar{c}) = 0$. A similar conclusion is drawn when the marginal frequencies are compared. This is depicted in Figure 3, which shows that the frequency at the onset of oscillatory Taylor–Couette flow increases (from zero) with the wave number, reaches a maximum, at the values ($De_{\min}, k_{\min}$), and then decreases asymptotically to zero as $k \to \infty$. Thus, periodic TVF appears to be easiest to detect, given its relatively maximum frequency, when it first sets in. Again, the two sets of curves in Figure 3 compare well for

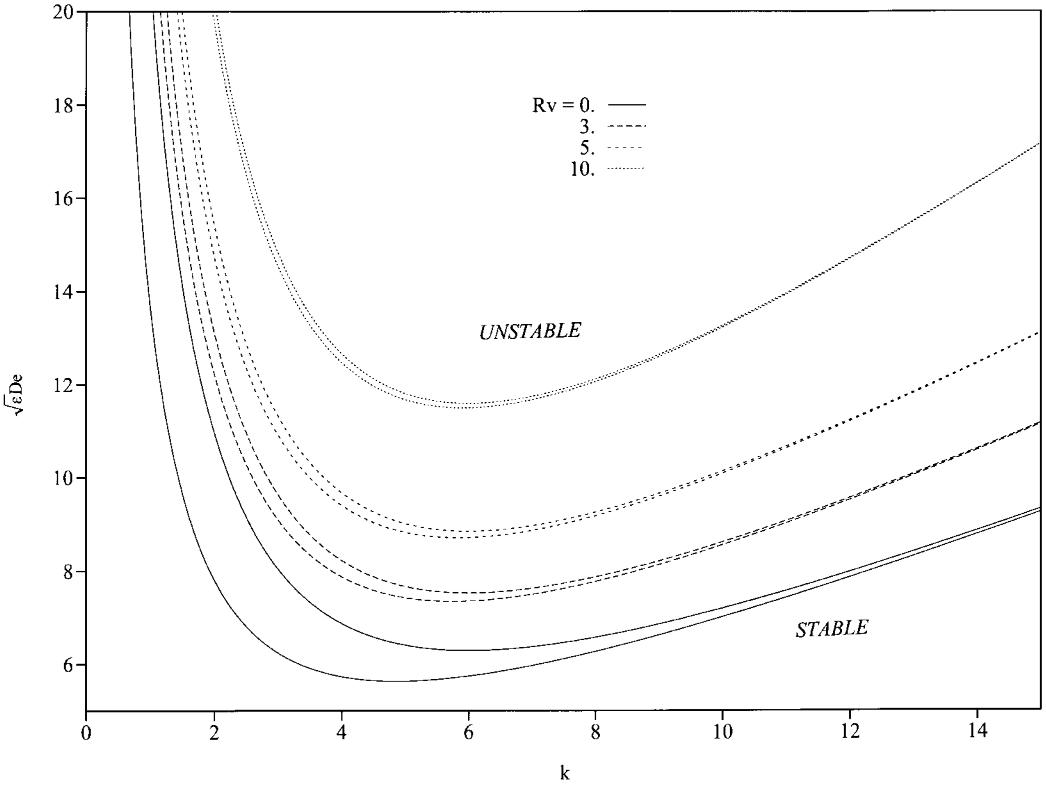

Figure 2. Marginal stability curves for the onset of purely elastic oscillatory TVF. Comparison between curves based on linear stability analysis (dashed curves) of system (B8) and those based on the approximate solution (solid curves) to Equation (37). The former lead slightly lower critical values.

$Rv > 2$ and large wave numbers. That the maximum in frequency coincides at the onset of the Hopf bifurcation is not difficult to prove since the frequency at the critical point is always of the form: $\omega_r \propto 1/De$, so that $\partial\omega_r/\partial k = 0$ whenever $\partial De/\partial k = 0$.

3.2. Stability of the Hopf bifurcation

Through the linear stability analysis above, various conditions for the existence of oscillatory TVF were established. It is found that the base (Couette) flow remains stable as long as De is below De_c, with De_c satisfying Equation (45). At $De = De_c$ the base flow loses its stability, but whether this loss of stability is always accompanied by an exchange of stability between the circumferential and periodic flow remains to be established. In other words, the emerging Hopf bifurcation may not be always stable. One is particularly interested in seeking conditions under which periodic behavior may not set in, and this depends on the values of k, Rv and ε when De slightly exceeds De_c. Since the bifurcation point is a nonhyperbolic fixed point, a regular perturbation expansion around it does not lead to the true stability picture. In this work, the method of multiple scales is used, similarly to thermal convection of viscoelastic fluids

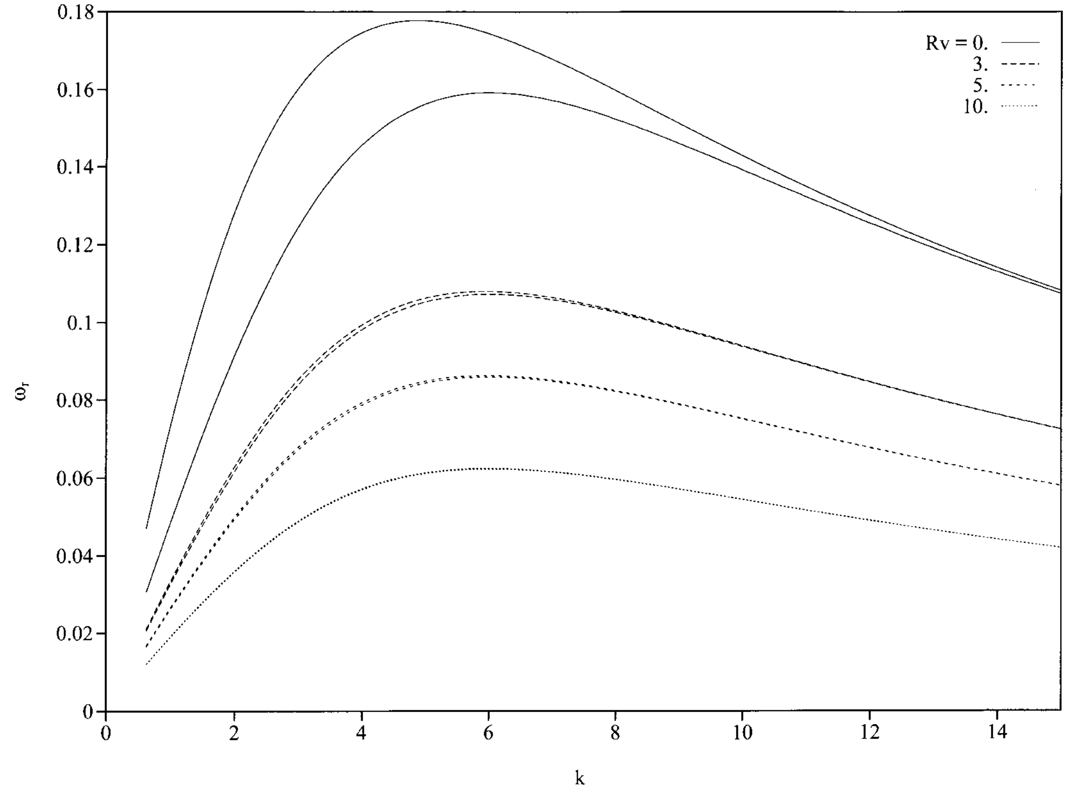

Figure 3. Frequency of limit cycle at the onset of purely elastic oscillatory TVF as function of the wave number. Curves based on similar solutions as in Figure 2.

[33]. Another alternative is to use center manifold theory [62–64], which was also applied for viscoelastic thermal convection [32]. The method of multiple scales is well documented elsewhere (see, for instance, Nayfeh and Balachandran [64]), and only details relevant to overstable Taylor–Couette will be given here.

Consider the bifurcation that occurs at $De = De_c(k = k_c)$ for a given viscosity ratio as shown in Figure 2. At the bifurcation point, two of the eigenvalues are complex-conjugate purely imaginary, $\pm i\omega_r$, and the rest of the roots are generally complex with negative real parts. The corresponding limit cycle has a period given by $2\pi/\omega_r$. In the vicinity of the bifurcation point (origin in phase space), the velocity and stress coefficients, which are governed by system (B8), are next approximated, thus allowing the determination of the limit cycle and its frequency as one departs from the fixed point. It is first convenient to recall system (B8):

$$\frac{\mathrm{d}x_i}{\mathrm{d}t} = F_i(x_1, \ldots, x_{20}; De), \quad i \in [1, 20] \tag{46}$$

where $x_i(t)$ are the stress coefficients given by Equation (B9). Note that in the absence of inertia only the stress coefficients are dependent variables since the velocity coefficients are expressible in terms of stresses. In this case, the Hopf bifurcation point becomes $(x_i = 0; De =$

De_c), $\forall i \in [1, 20]$. The departure from the bifurcation point is then introduced as:

$$x_i = \delta y_i, \quad i \in [1, 20] \quad \text{and} \quad De - De_c = \delta^2 \alpha \tag{47}$$

where δ is a small dimensionless ordering parameter, which should not necessarily be identified with the gap-to-radius ratio, ε, and will be set equal to unity at the end of the analysis. Substituting Equation (47) into Equation (46), expanding the right-hand side(s) in Taylor series for small $\|\mathbf{y}\|$ and small $|\alpha|$, and using the fact that $F_i(0, \ldots, 0; De_c) = 0$, one obtains

$$\frac{\mathrm{d}y_i}{\mathrm{d}t} = F_{i,j} y_j + \delta F_{i,jk} y_j y_k + \delta F_{i,De} \alpha + O(\delta), \quad i \in [1, 20] \tag{48}$$

where a repeated index denotes summation over the index and a comma means partial differentiation. To determine an approximation to the limit cycle, one introduces another time scale $T = \delta^2 t$ and seeks expansions of the form:

$$y_i = y_i^1(t, T) + \delta y_i^2(t, T) + \delta^2 y_i^3(t, T) + O(\delta^2), \quad i \in [1, 20] \tag{49}$$

Substituting Equation (49) into Equation (48) and equating coefficients of like powers of δ leads to the nondecaying solution for $\mathbf{y}_i^1$ of the form:

$$y_i^1(t, T) = A(T) p_i e^{i\omega t} + A^*(T) p_i^* e^{-i\omega t} \tag{50}$$

where p_i are the components of the right eigenvector of the 20×20 Jacobian matrix $F_{i,j}$ of F_i evaluated at $(0, \ldots, 0; De_c)$. $A(T)$ is a complex function that is determined upon elimination of the secular terms, leading to the following amplitude equation [65]:

$$\frac{\partial A}{\partial T} = \alpha \beta_1 A + 4\beta_2 A^2 A^* \tag{51}$$

where $\beta_1 = \beta_{1r} + i\beta_{1i}$ and $\beta_2 = \beta_{2r} + i\beta_{2i}$ are complex quantities given in Appendix C. Although the solution of Equation (51) determines the amplitude of the limit cycle near the bifurcation point, it is the value of and, more importantly, the sign of the ratio β_{1r}/β_{2r} that are of interest since they determine the stability of the limit cycle.

Indeed, β_{1r}/β_{2r} represents the slope of the Hopf bifurcation near the fixed point in the $(|A|, De)$ plane, and the limit cycle is stable (unstable) if β_{1r}/β_{2r} is negative (positive). Figure 4 displays the value of β_{1r}/β_{2r} as function of the critical wave number, k_c, for various values of the viscosity ratio Rv for $\varepsilon = 0.0625$. This particular value of the gap-to-radius ratio corresponds to the Taylor–Couette apparatus used by Muller *et al.* [1], which will be referred to extensively below. The figure shows that β_{1r}/β_{2r} can be positive when Rv is small, but that, overall, it is negative. It appears, for the range of parameters investigated, that β_{1r} is always positive and that β_{2r} may change sign as k_c or Rv are varied. Typically, for $Rv < 0.3$, the limit cycle appears to be stable for the lower range of k_c values. When k_c increases (for given Rv), there is a change in the stability picture as β_{1r}/β_{2r} becomes singular. At this point β_{2r} is zero and switches sign to become positive. The point of discontinuity is shifted to higher k_c values as Rv increases. For $Rv > 0.3$, the limit cycle appears to be always stable, but the overall influence of Rv is not necessarily consistent.

The influence of the viscosity ratio is depicted in Figure 5, which displays the behavior of β_{1r}/β_{2r} as function of Rv for four values of k_c and $\varepsilon = 0.0625$. The figure shows that β_{1r}/β_{2r} is negative, each curve exhibits a minimum that tends to be stronger as k decreases. The ratio

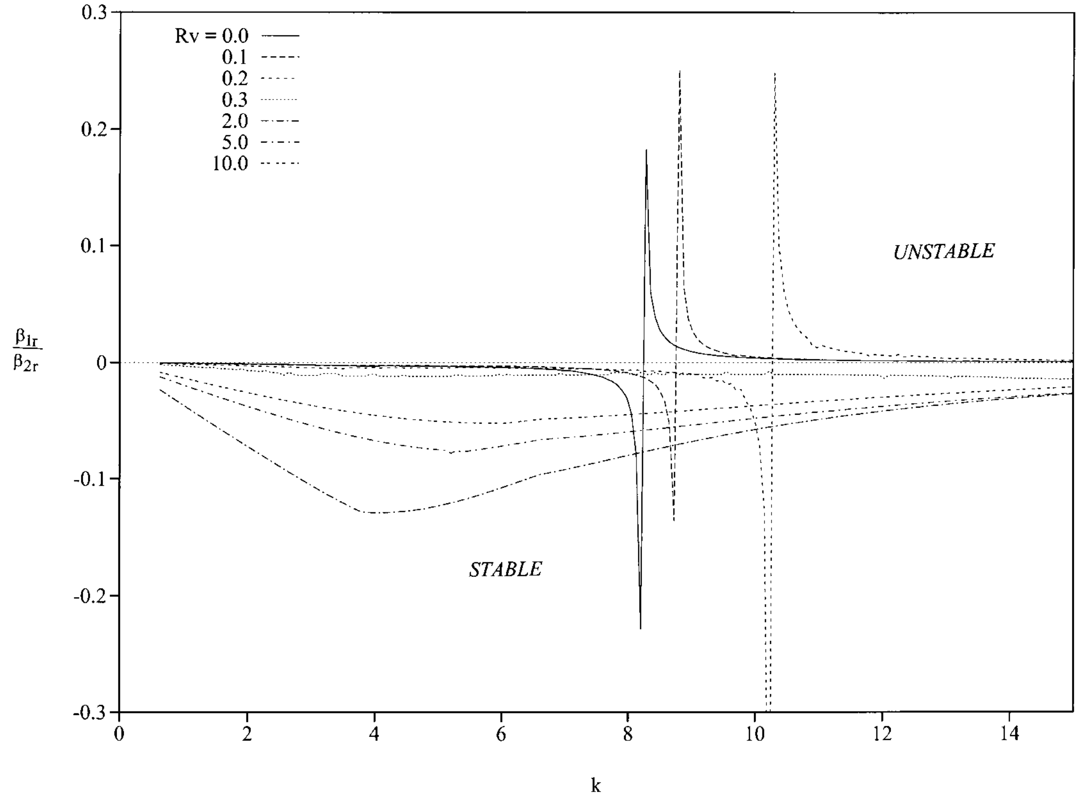

Figure 4. Influence of the wave number on the stability of the limit cycle near the bifurcation point. For given viscosity ratio, *Rv*, the limit cylce is stable (unstable) when the ratio β_{1r}/β_{1i} is negative (positive).

tends generally asymptotically to zero as $k \to \infty$. As to the effect of ε, the gap-to-radius ratio does not seem to have any influence on the stability picture. This is confirmed in Figure 6, which shows the behavior of β_{1r}/β_{2r} as function of k for various ε values and $Rv = 0.2$.

4. FINITE AMPLITUDE ELASTIC OVERSTABILITY AND COMPARISON WITH EXPERIMENT

Linear stability analysis, such as the one presented in the previous section, determines the flow field as it departs slightly from the base flow. However, it fails to give the flow structure for a large disturbance. The influence of the nonlinear terms must thus be examined through the numerical solution of system (B8). The influence of elasticity or normal stress effects will be examined in some detail. The behavior of highly elastic fluids with negligible inertia is particularly considered as the elasticity level is increased beyond the critical value for loss of stability of the base flow. The flow will be examined as overstability (oscillatory TVF) sets in, and it will be seen how nonlinearity affects the subsequent flow by determining the

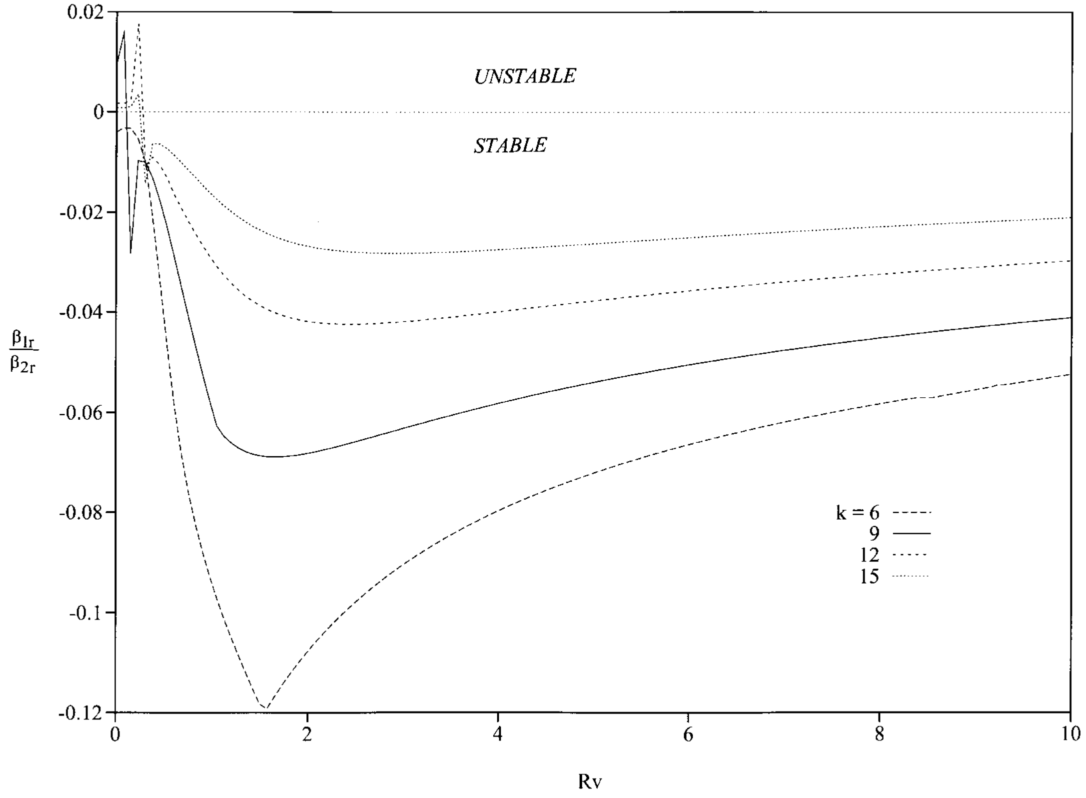

Figure 5. Influence of the viscosity ratio on the stability of the limit cycle near the bifurcation point. For given wave number, k, the limit cylce is stable (unstable) when the ratio β_{1r}/β_{1i} is negative (positive).

temporal flow behavior and corresponding power spectrum. The present nonlinear behavior will also be compared with the experiment of Muller *et al.* [1], which was conducted for a highly elastic fluid under conditions of vanishingly small inertia.

Muller *et al.* [1] conducted Laser Doppler velocimetry (LDV) measurements of the axial velocity component of a highly elastic (Boger) fluid (a polyisobutylene-based solution) placed between two concentric cylinders ($\varepsilon = 0.0625$), with the outer cylinder being at rest, and the inner cylinder rotating at constant angular velocity, Ω. The velocity signature shows an oscillatory flow at a vanishingly small Reynolds number. The flow appears to undergo a transition from the purely azimuthal Couette flow to time periodic TVF as De exceeds a critical value, De_c, say, which is in good agreement with the value predicted by the earlier linear stability analysis of an Oldroyd-B fluid [8]. The LDV measurements show that the oscillatory behavior is not localized but appears to be spread throughout the flow. As De increases from the critical value, the amplitude of oscillation increases like $(De - De_c)^{1/2}$. The corresponding power density spectrum shows peaks, which are instrumentally sharp at the fundamental frequency, the growth of harmonics, and eventually subharmonics, reflecting, perhaps, the presence of a period doubling or quasiperiodic motion. However, the emergence of subharmonics appears

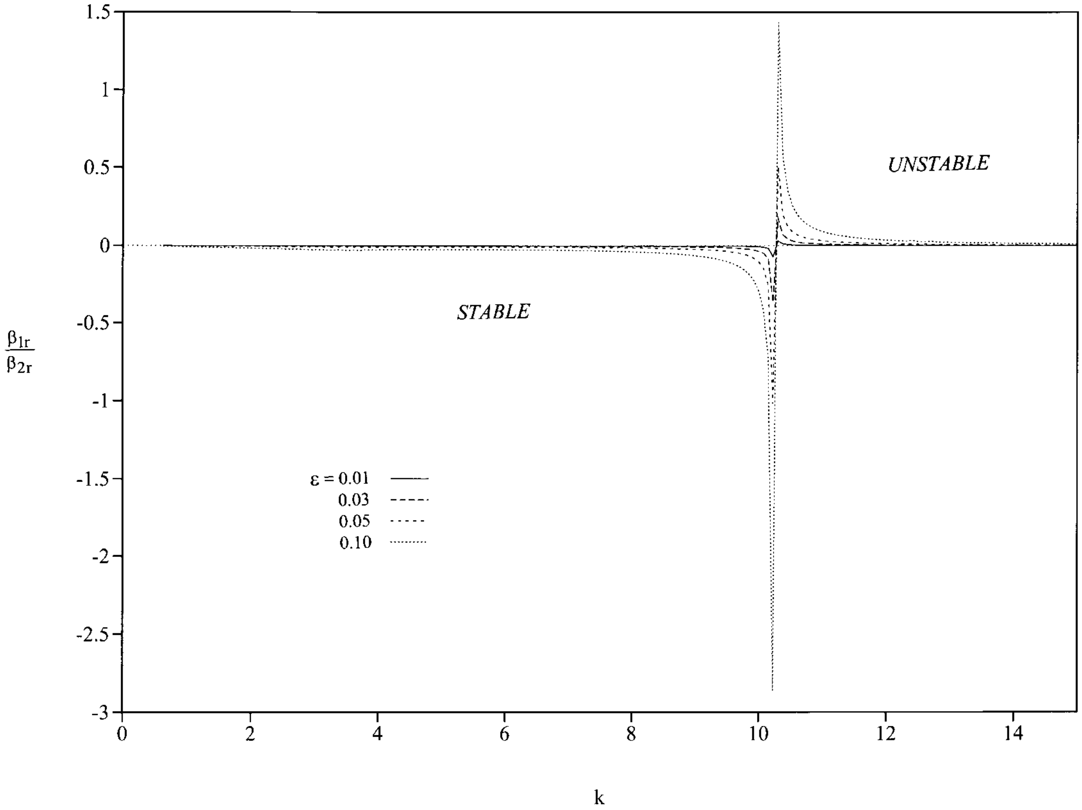

Figure 6. Influence of the gap-to-radius ratio, ε, on the stability of the limit cycle near the bifurcation point.

to be incorrect from later studies. Although the finite-element calculations of Northey *et al.* [40] predicted the emergence of finite amplitude overstability for a UCM fluid, these authors, reported having numerical difficulties in obtaining the solution at the higher Deborah numbers (possibly coinciding with the onset of period doubling). Their calculations are thus limited to an extremely narrow range of postcritical Deborah numbers. Khayat's previous work [35] confirms the existence of a stable Hopf bifurcation for $De > De_c$ which loses its stability at some De value coinciding with the onset of a series of period doublings. At the cumulation point, the velocity signature, phase space trajectory and power spectrum indicate the onset of chaotic behavior. The present work attempts to reproduce the experimentally observed finite amplitude elastic overstability for an Oldroyd-B fluid by adopting a nonlinear dynamical systems approach as formulated in the previous sections.

Experimental results show an oscillatory flow at $Re \sim 7 \times 10^{-3}$. The flow appears to undergo a transition from the purely azimuthal CF to time periodic TVF as De exceeds a critical value. The LDV measurements show that the oscillatory behavior is not localized but appears to be spread throughout the flow. As De increases from the critical value, the amplitude of oscillation increases. The corresponding power density spectra show peaks, which are instrumentally sharp at the fundamental frequency, the growth of harmonics, and eventually subharmonics, reflecting the possible presence of period doubling or emergence of a second fundamental frequency. Additional experiments at relatively high Deborah number are, however, needed in order to determine the possible route(s) to chaotic or turbulent motion.

One cannot expect full quantitative agreement between theory and experiment given the assumptions made in the formulation, particularly, the level of approximation in the solution representation, the narrow-gap limit, and the Oldroyd-B constitutive model. Moreover, the wave number k needs to be imposed since it cannot be theoretically determined. This quantity is also not known from experiment in the present case; the wave number is difficult to establish under transient conditions of flow [60, 61]. Other parameters and variables are also difficult to obtain from the experiment and will have to be somewhat speculated as it will next argued.

Attention is focused on the flow conditions as examined in the experiment of Muller *et al.* [1], and attempt is made to determine the values of the various dimensionless group parameters introduced in system (B8). Not all flow parameters needed for theory are explicitly reported from experiment. The test fluid used in the experiment has a (constant) viscosity of 162 poise, and consists of 1000 ppm of a high molecular weight polyisobutylene dissolved in a viscous, low molecular weight polybutene of viscosity 128 poise, so that the solvent-to-polymer viscosity ratio $Rv = 3.76$. The fluid relaxation time λ_1 varies depending on which rheological technique is used to measure it, but its value ranges roughly from 3.3 to 10.9 s [1, 60, 61]. The inner and outer cylinder radii were 8 and 8.5 cm, respectively, so that $\varepsilon = 0.0625$. Although the inner cylinder angular velocity, Ω, was not explicitly given in the experiment, its value can still be inferred from the value of the experimental Deborah number, De_{M}, which was introduced by Muller *et al.* [1] as: $De_{\mathrm{M}} = [(2\Omega\lambda_1(1+\varepsilon)^2)/((1+\varepsilon)^2-1)]$. Note that $De_{\mathrm{M}\varepsilon\to 0} = De$. It appears that there was only one fluid used throughout the experiment, and De_{M} was thus varied in the experiment by varying only the inner cylinder speed, Ω. Hence, from the range of values of De_{M} reported in the experiment, the corresponding values of the inner cylinder speed are given by $\Omega = De_{\mathrm{M}}/77.06$ for $\lambda_1 = 4.4$ s and $\varepsilon = 0.0625$. Muller *et al.* [1] reported that the highest Reynolds number reached in the experiment was of the order 7×10^{-3}. Indeed, if one takes the same definition of the Reynolds number used in the experiment, namely $Re = [(\rho\Omega R_i d)/(\eta)]$, and considers the value of Ω corresponding to the highest Deborah number reported ($De_{\mathrm{M}} = 54.5$), one finds that $Re = 2.86\times10^{-3}$ (assuming the density $\rho = 1\ \mathrm{g/cm}^3$). As mentioned earlier, the experimental wave number, k, at which overstability occurs, is not reported by Muller *et al.* [1]; its measurement may be difficult under transient conditions. Its exact value, however, is not crucial in this case since it is likely that the critical Deborah number for the onset of overstability does not depend strongly on the wave number in the range $k \in [4, 8]$ for $Rv = 3.76$ as theory suggests; this is reflected by the flattening of the neutral stability curves around the critical value $De_{\min}$ of the Deborah number (see Figure 2). The wave number will be fixed to $k = 4.85$ for all subsequent calculations. This is slightly lower than the minimum value $k_{\min} = 5.8$ of the wave number, which corresponds to $De_{\min} = 31.52$ predicted by the present linear stability analysis. The value $k = 4.85$ is close to wave numbers reported in other experiments on Taylor–Couette flow of viscoelastic fluids [60, 61]. Thus, similarly to the experiment, only the Deborah number will be varied (by varying Ω) in the following calculations and results.

The flow is now examined as De is increased from zero, that is from the Newtonian level. Referring to Figure 2, it is seen that, for a given Rv, the Couette flow is unconditionally stable to any perturbation as long as De is below the critical value. Note that for $Rv = 3.76$, $k = 4.85$ and $\varepsilon = 0.0625$, the critical Deborah number is equal to $De_c = 32$ at which the base flow loses its stability. In the absence of inertia, and in contrast to the Taylor–Couette flow of a Newtonian fluid, an exchange of stability takes place between the circular Couette flow and oscillatory TVF since no steady TVF can set in [35]. In order to compare the present results with experiment, dimensional quantities are used. It is thus important to point out the manner in which the main variable of interest, namely, the axial velocity signal, is obtained from the solution of system (B8). Once the coefficients related to the radial velocity are obtained, the dimensionless axial velocity component is determined. In dimensional form one has:

$$U_Z(x,z,t) = -\frac{R_i\Omega}{k}\sin(kz)[\lambda u_x^{11}(t)\Phi_1^p(x) + \mu u_x^{12}(t)\Phi_2^p(x)] \equiv -W(x,t)\sin(kz) \qquad (52)$$

Note that x, z and t remain dimensionless. In the experiment of Muller *et al.* [1], the evolution of the axial velocity was measured at $x = 1/4$. Thus, for comparison between theory and experiment, the evolution of the spatial amplitude of the axial velocity, $W(1/4,t)$. is evaluated. The experimental critical value of the Deborah number, at which oscillatory motion was first detected, is reported to be equal to 32.3, and happens to be slightly larger than the theoretical value, $De_c = 32$, predicted by linear stability analysis. This disagreement may be only apparent, and may be justified if one notes that the experimental critical value is extremely difficult to measure accurately. It is simply difficult to detect experimentally small amplitude oscillatory TVF as De just exceeds De_c. This is also true for the theoretical calculations; the oscillatory behavior was only detected as De exceeded 32. In fact, at $De = 32$, the amplitude of oscillatory signal for $W(1/4,t)$ is $O(10^{-5})$ cm/s. The velocity signature and corresponding power density spectrum are shown in Figure 7 for $De = 32$. The scales in this and subsequent figures are the same. Insets are also included showing the behavior on much smaller scales. It is thus reasonable to claim that the predicted and experimental critical Deborah numbers are practically equal.

As De is increased from the critical value, the amplitude of oscillation increases, confirming the existence and the stability of the Hopf bifurcation, in agreement with the multiple scales analysis above and experiment [1]. The resulting sequence of flows is shown in Figures 8–11 for the same range of Deborah numbers as in the experiment: $32 < De < 50$, and should be compared with that reported in Figures 6 to 9 of Muller *et al.* [1]. Note the different definition of the Deborah number used by Muller *et al.* [1], De_M, defined above. In the present problem, $\varepsilon = 0.0625$, and $De = 0.911 De_M$. Each figure shows the time evolution of $W(1/4,t)$ and corresponding power spectrum for the same Deborah numbers reported from experiment. At $De = 32.5$ (Figure 8), the velocity signature and corresponding Fourier spectrum display periodic motion after the purely circular (Couette) flow becomes unstable. The amplitude of oscillation remains relatively small (0.008 cm/s). The power spectrum indicates the presence of a dominant frequency of 0.02 Hz and a weak second harmonics. This periodic behavior persists as De increases, as depicted in Figure 9 for $De = 35$, with the flow always oscillating around the origin (Couette flow). At $De = 43.57$ (Figure 10), the motion remains periodic around the origin, with an increase in amplitude to 0.052 cm/s. There is an increase in the fundamental frequency to 0.0298 Hz and the emergence of four significant even and odd harmonics. This trend persists as De is further increased with the eventual emergence

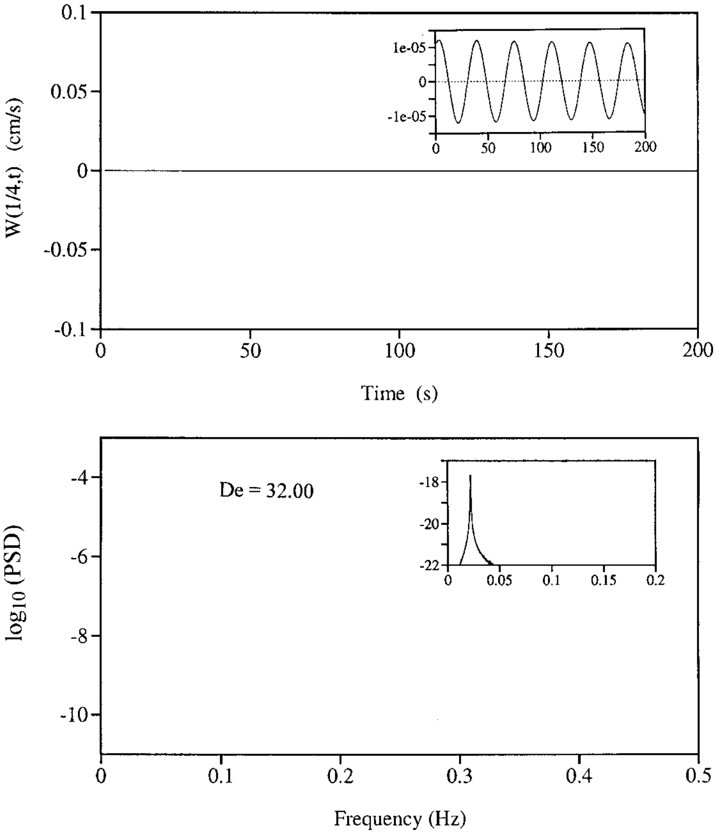

Figure 7. Elastic overstability for a Boger fluid at $De = 32$ ($Rv = 3.76$, $\varepsilon = 0.0625$ and $k = 4.85$). The figure shows the time signature and power spectrum of the axial velocity at $x = \frac{1}{4}$ as oscillatory behavior is first detected (insets). The scales used are the same as in subsequent figures.

of additional harmonics. This is clearly depicted in Figure 11 for the highest Deborah number considered in the experiment: $De = 49.65$.

In sum, the sequence of flows predicted by the present model is clearly comparable to that reported by Muller *et al.* [1]. Experiment predicts a loss of stability of the origin at a critical Deborah number equal to 32.3, while the present calculations suggest that oscillatory TVF sets in at $De = 32$. Both theory and experiment predict the increase in amplitude of the velocity signal, the emergence of higher harmonics in the Fourier spectrum. Unlike our previous qualitative comparative studies [35], the present comparison leads to good quantitative agreement between theory and experiment in the postcritical Taylor–Couette flow. This confirms that, although qualitative agreement is achieved regardless of the type of boundary conditions used, the use of rigid–rigid boundary conditions appears to lead to the accurate quantitative picture. The agreement between theory and experiment is further evidenced from the bifurcation and frequency diagrams.

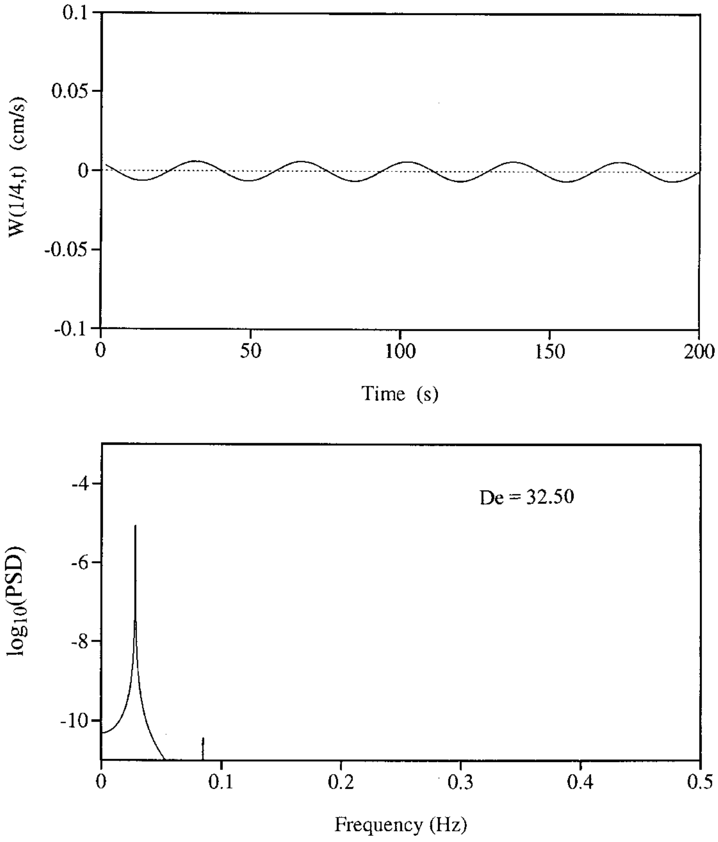

Figure 8. Time signature and power spectrum of the axial velocity at $x=\frac{1}{4}$ for a Boger fluid at $De=32.5$ ($Rv=3.76$, $\varepsilon=0.0625$ and $k=4.85$).

Figure 12 shows the Hopf bifurcations for the square of the velocity amplitude based on the present model, and the measurements from Muller *et al.* [1]. In the figure, the experiment and numerical calculation show the onset of periodic motion as the Deborah number exceeds the critical value ($De_c \approx 32$). Both sets of data show that the amplitude of oscillation grows like $(De - De_c)^{1/2}$ in agreement with the prediction based on asymptotic analysis in the limit $De \rightarrow De_c$. Figure 13 displays the dependence of the dominant frequency and its harmonics on the Deborah number. The frequency tends to increase with De almost linearly. Unlike the amplitude, the frequency exhibits a jump at the critical Deborah number. This means that any initial weak velocity amplitude at the onset of oscillatory TVF has a dominant frequency that is relatively easy to detect. The agreement between the computed and measured frequencies is obvious from the figure. The apparent growing disagreement for the higher harmonics is to be expected. Any initial discrepancy at the dominant frequency level is simply amplified as it is multiplied by two for the second harmonics, by three for the third harmonics and so on.

It is important to emphasize that there is very good agreement between theory and experiment despite the approximations and uncertainties in the present formulation. Assumptions

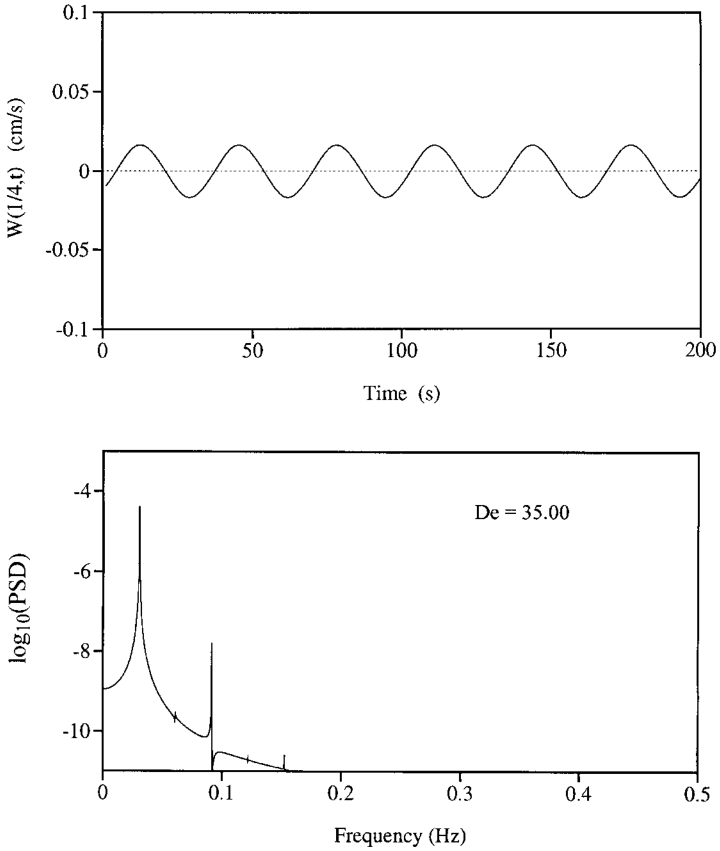

Figure 9. Time signature and power spectrum of the axial velocity at $x = \frac{1}{4}$ for a Boger fluid at $De = 35$ ($Rv = 3.76$, $\varepsilon = 0.0625$ and $k = 4.85$).

such as the narrow-gap limit and the infinite length of the two cylinders cannot but make the theory approximate. The uncertainties come mainly from not knowing the axial wave number accurately, and the constitutive behavior of the test fluid used in the experiment. To our knowledge, this is closest agreement between theory and experiment that has so far been achieved for the TCF of highly elastic fluids.

5. DISCUSSION AND CONCLUDING REMARKS

In this study, a low-dimensional nonlinear dynamical system approach is adopted for the simulation of the narrow-gap TCF of highly elastic fluids of the Oldroyd-B type. This rather elementary constitutive model is adopted for three main reasons. First, since the aim of the study is to examine the influence of elasticity on the onset and stability of TVF, the use of the Oldroyd-B model becomes justified for a class of the so-called Boger fluids for which the viscosity is sensibly constant over a wide range of shear rates with the corre-

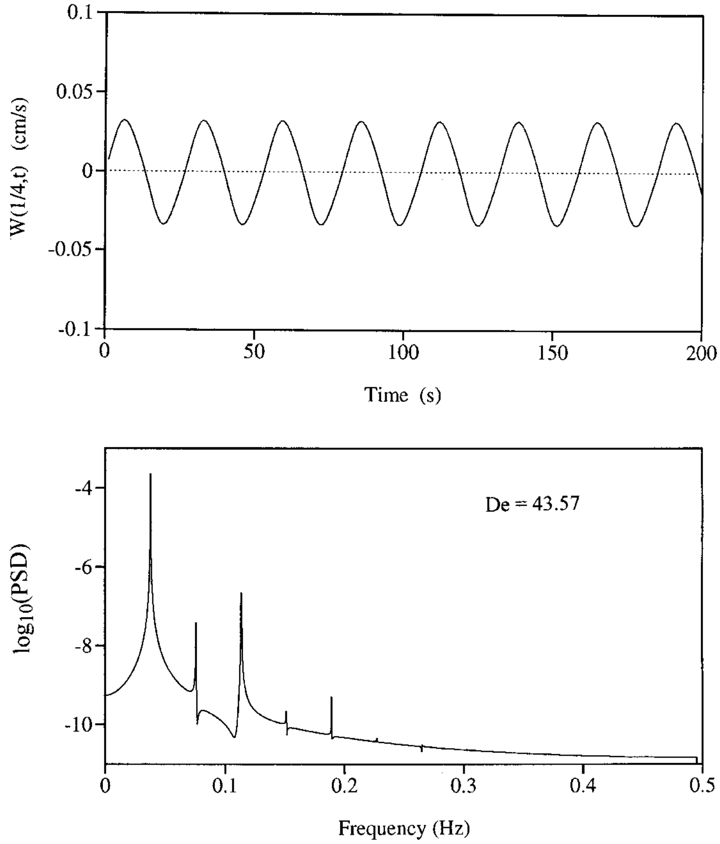

Figure 10. Time signature and power spectrum of the axial velocity at $x=\frac{1}{4}$ for a Boger fluid at $De=43.57$ ($Rv=3.76$, $\varepsilon=0.0625$ and $k=4.85$).

sponding normal stress levels nevertheless substantial. A polyacrylamide solution in a maltose syrup/water mixture typically constitutes such a fluid [66]. Thus, the influence of shear thinning, or, more generally, the dependence of the fluid parameters on the rate-of-strain tensor may be neglected. Second, the Oldroyd-B constitutive equation is one of the simplest viscoelastic laws that accounts for normal stress effects (which lead to the so-called Weissenberg rod-climbing phenomenon). Other more realistic phenomenological [6, 67] or molecular-theory based models [6, 68–70] are more difficult to handle, and are likely to lead to a stability picture different from the one predicted by the present analysis. For instance, the presence of shear thinning, which is not accounted for by the Oldroyd-B equation, will likely have a destabilizing effect since the *effective* Reynolds number increases as the viscosity decreases with increasing shear rate [34, 37, 46]. Other more complicated constitutive equations accounting for the nonlinear dependence of the transport coefficients on the rate-of-strain tensor may also be examined. The present formulation accounts for nonlinearities stemming only from the convective and upper-convective terms in the constitutive equation. Third, the formulation and method of solution are validated upon comparison with the ex-

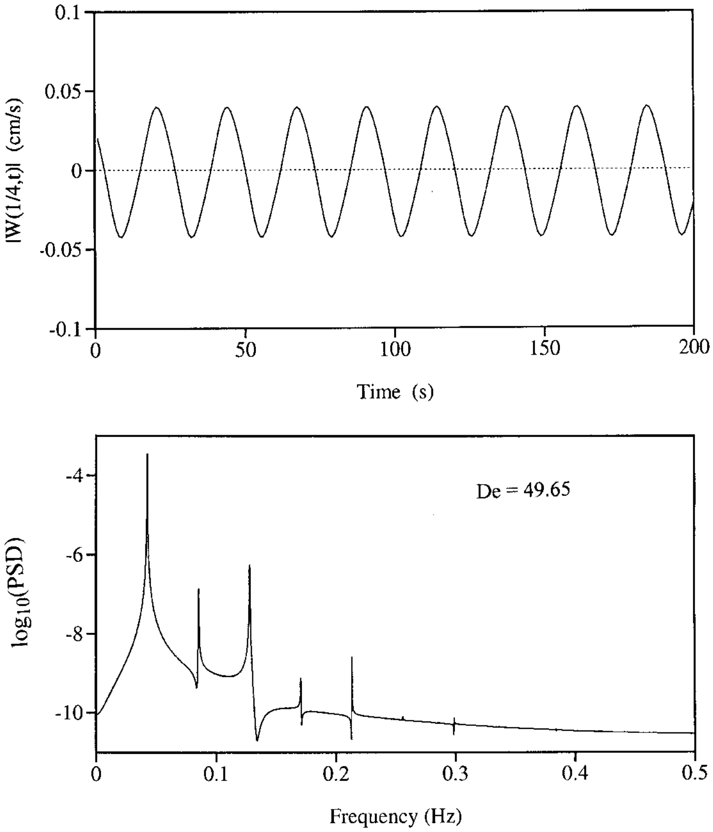

Figure 11. Time signature and power spectrum of the axial velocity at $x=\frac{1}{4}$ for a Boger fluid at $De=49.65$ ($Rv=3.76$, $\varepsilon=0.0625$ and $k=4.85$).

periment of Muller *et al.* [1], which was conducted for a Boger fluid in the absence of inertia.

The nonlinear dynamical system is derived by expanding the flow field (velocity, pressure and stress) into suitably selected Fourier modes along the axial direction, and Chandrasekhar functions in the radial direction. The time-dependent expansion coefficients are evaluated by applying the Galerkin projection of the various modes onto the conservation and constitutive equations, and adopting a suitable truncation to close the hierarchy of the resulting set of ordinary differential equations. The influence of higher order stresses is assessed upon comparison with the analytical solution of the linearized equations, and with experiment in the nonlinear regime of postcritical TVF. It is concluded that 20 independent modes in stress are sufficient to obtain an accurate solution. Because of the absence of inertia effects, the velocity coefficients are explicitly expressible in terms of the stresses. The more severe truncation level used in our previous work [35] led to a six-dimensional system, which was derived by neglecting normal stress terms that tend to become significant for highly elastic flows. The present model (B8), which, in contrast to the previous model, is based on the more realistic

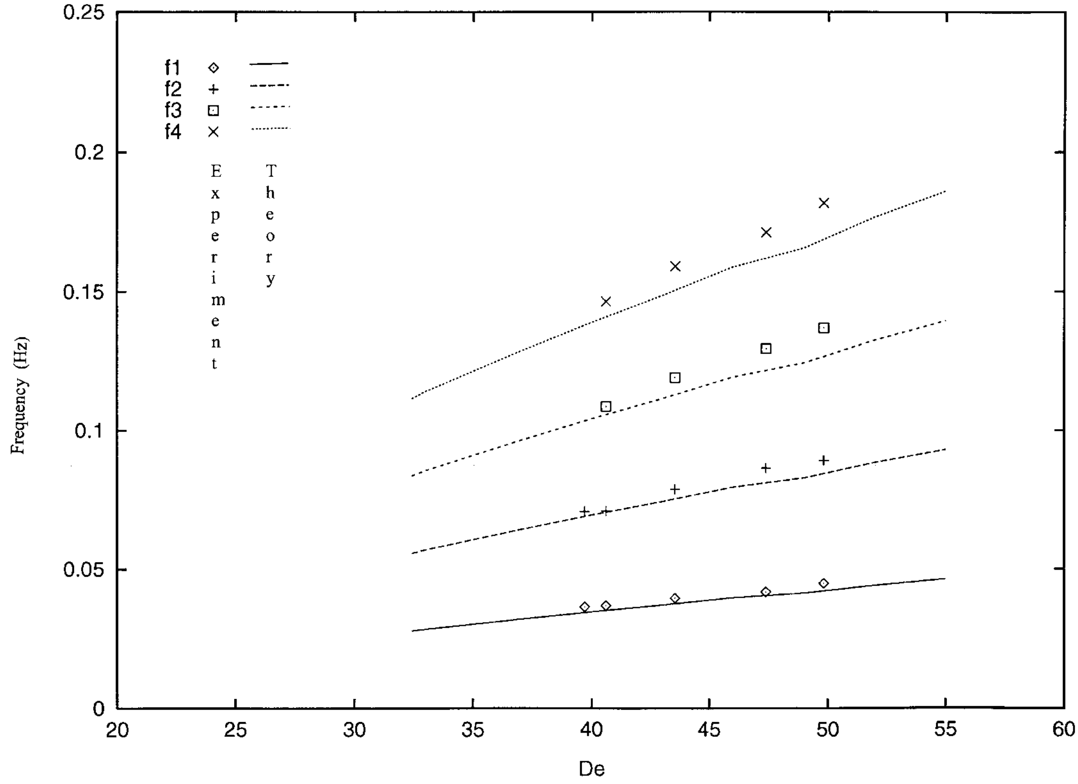

Figure 12. Bifurcation diagram and comparison between theory (dashed line) and experimental measurements (diamonds) of Muller *et al.* [1]. The figure shows the square of the amplitude of axial velocity at $x = \frac{1}{4}$ as a function of the Deborah number.

rigid–rigid boundary conditions, takes into account more effectively the influence of normal stresses, and is thus adequate to describe the flow of a highly elastic fluid (with negligible inertia). The inclusion of higher order stress terms and the more realistic boundary conditions allow direct comparison with the experiment of Muller *et al.* [1].

As mentioned above, a judicious selection process of the most influential modes was carried out to ensure that the relevant dynamics is captured by the approximate model and solution. This was first done by referring to the results from linear stability analysis of Equation (34) and the more approximate system (B8). The exact solution was obtained using the direct method, and was compared to the approximate solution based on the Fourier/Chandrasekhar expansion for the eigenvalue problem (34)–(36). Since inertia is absent, Equations (A2)–(A16) reduce to the simple constant coefficient Equation (34). Only two modes, given by Equation (40), are needed in the approximate solution, leading to good agreement with the exact solution (37), especially in the lower wave number range (Figure 1). Similar marginal curves were also obtained from the linearization of (B8) (see Figure 2).

Linear stability predicts that the base (Couette) flow loses its stability via a Hopf bifurcation as the Deborah number, *De*, reaches a critical value De_c (for a given wave number). Thus,

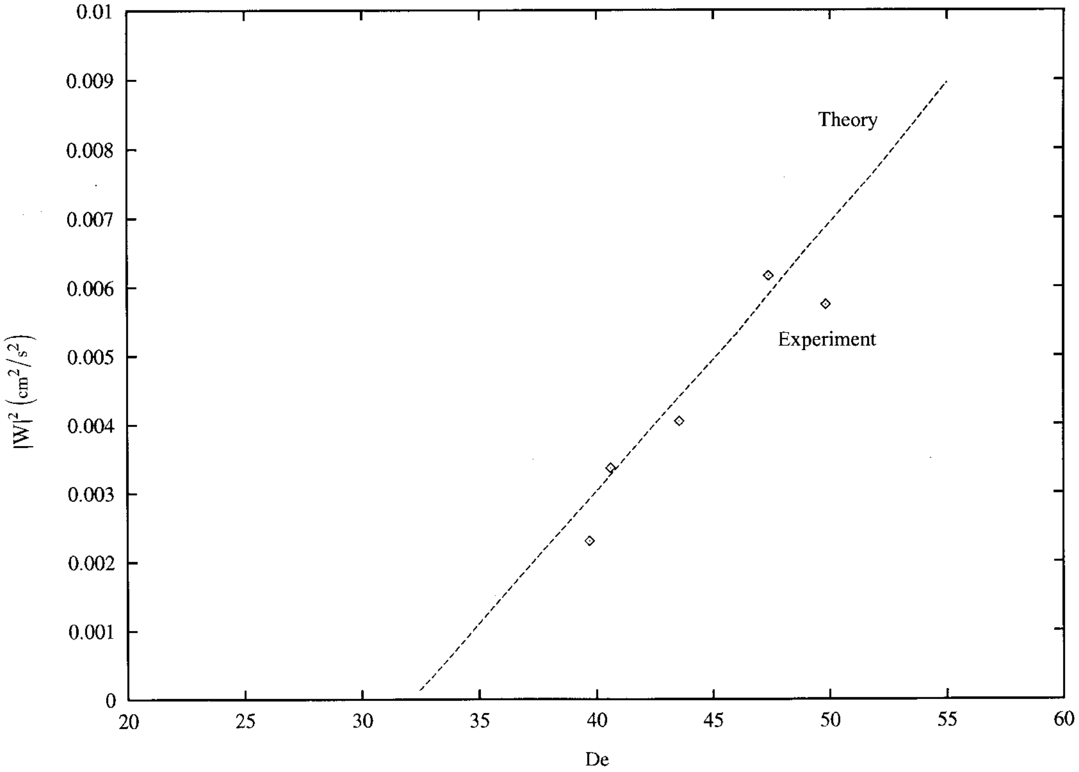

Figure 13. Frequency of oscillation and comparison between theory (continuous lines) and experimental measurements (symbols) of Muller *et al.* [1]. The figure shows the frequency of axial velocity at $x=\frac{1}{4}$ as a function of the Deborah number.

unlike inertia induced steady TVF that sets in at a critical Reynolds number, purely elastic Couette flow may lose its stability to an oscillatory TVF. This prediction is in agreement with the linear analysis of Larson *et al.* [8] and confirms the experimental observation of Muller *et al.* [1]. The conditions for stability of the emerging limit cycle are examined using the method of multiple scales. It is found that the limit cycle is stable under practical conditions of flow. Unlike the previous model [1], the present system (B8) leads to good agreement with experiment. To the author's knowledge, the results reported in Figures 12 and 13 constitute the closest qualitative and quantitative agreement between theory and the experiment of Muller *et al.* [1] to be achieved.

The present theory predicts the sequence of periodic behaviors observed as the Deborah number is increased: (1) loss of stability of the base flow to an oscillatory flow at a critical Deborah number ($De_c=32$ as predicted by the model vs 32.3 from experiment), (2) growth of amplitude of the velocity signature like $(De-De_c)^{1/2}$, in agreement with asymptotic analysis, (3) the emergence of higher harmonics in the Fourier spectrum as De is further increased.

A closer quantitative agreement between theory and experiment can hardly be envisaged given the uncertainty surrounding experimental conditions, on the one hand, and the various assumptions that will likely plague any viscoelastic numerical simulation in the nonlinear range: existence of a spectrum of relaxation times, difficulty in determining (experimentally) the various rheological parameters for a given constitutive model, the nonlinear dependence of transport coefficients on the rate of strain tensor, and so on. Moreover, the sources of discrepancy between theory and experiment are generally the very limitations of both Newtonian and viscoelastic flow formulations. The lack of a theory capable of predicting the value of the axial wave number k constitutes a major difficulty. The prediction of the value of k remains an unresolved issue, and it is usually simply imposed in a theory from experimental observation. In the case of viscoelastic Taylor–Couette flow, however, the measurement of k is extremely difficult under transient flow conditions [60, 61]. Another source of discrepancy stems from end effects in the Taylor–Couette apparatus that have been neglected in the present formulation. The narrow-gap approximation is also a limiting assumption. Inertia effects can also play an influential role despite the fact that the experiment was conducted at a vanishingly small Reynolds number ($Re < 10^{-3}$). In general, the presence of inertia, no matter how small it may be, prohibits the base flow from losing its stability to the overstable mode. Instead, the base flow loses its stability first to *steady* (and not oscillatory) TVF since there is always a finite range of Re values over which the branches corresponding to steady TVF are stable.

In conclusion, a more appropriate model for highly elastic fluids is derived in the present work. It includes higher order normal stress terms. It is shown that purely elastic overstability can only be predicted if the higher order normal stress terms, which were neglected in the previous formulation [35], are properly accounted for. Particularly, the addition of the azimuthal normal stress component leads to additional coupling with higher order eigenmodes that can no longer be neglected. The resulting nonlinear dynamical system involves 20 instead of six degrees of freedom. Although more cumbersome, and therefore less amenable to eloquent algebraic manipulations, the expanded model (B8) is more accurate in its predictions, and leads to good quantitative agreement with linear stability analysis and experiment.

APPENDIX A: ELIMINATION OF THE *Z* DEPENCE

Equations (13)–(22) are now reduced upon projecting them onto the modes in the z direction. In this work, the zeroth- and first-order terms, u_i^0, p^0 and τ_{ij}^0, and u_i^1, p^1 and τ_{ij}^1 $(i,j=x,y,z)$, respectively, are retained from expansions (27)–(33). Upon substitution of the solutions (27)–(33) into Equations (13)–(22), and integrating over the interval $[0,\pi/k]$, it is found that the zeroth-order terms of the radial and axial velocity components, subject to boundary conditions (23), vanish, so that

$$u_x^0(x,t) = u_z^0(x,t) = 0 \tag{A1}$$

while the pressure coefficient $p^0(x,t)$ is decoupled from the rest of the flow variables, and therefore will not be considered any further. The remaining coefficients are governed by the following equations:

$$u_{x,x}^1 + ku_z^1 = 0 \tag{A2}$$

$$\tau_{xx,x}^1 + k\tau_{xz}^1 + p_{1,x} - \tau_{yy}^1 - aRv(u_{x,xx}^1 - k^2u_x^1) = 0 \tag{A3}$$

$$\tau^0_{xy,x} - aRvu^0_{y,xx} = 0 \tag{A4}$$

$$\tau^1_{xy,x} + k\tau^1_{yz} - aRv(u^1_{y,xx} - k^2 u^1_y) = 0 \tag{A5}$$

$$\tau^1_{xz,x} - k\tau^1_{zz} - kp_1 - aRv(u^1_{z,xx} - k^2 u^1_z) = 0 \tag{A6}$$

$$\tau^0_{xx,t} + u^1_x \left(\frac{1}{2}\tau^1_{xx,x} + k\tau^1_{xz}\right) - \frac{k}{2} u^1_z \tau^1_{xx} - u^1_{x,x}\tau^0_{xx} = -De^{-1}\tau^0_{xx} \tag{A7}$$

$$\tau^1_{xx,t} + u^1_x \tau^0_{xx,x} - 2u^1_{x,x}\tau^0_{xx} = -De^{-1}(\tau^1_{xx} + 2au^1_{x,x}) \tag{A8}$$

$$\begin{aligned} &\tau^0_{yy,t} + \frac{1}{2}(u^1_x \tau^1_{yy,x} - ku^1_z \tau^1_{yy}) \\ &\quad -2\varepsilon\left[u^0_{y,x}(\tau^s_{xy} + \tau^0_{xy}) + \tau^0_{xy}u^s_{y,x} + \frac{1}{2}(u^1_{y,x}\tau^1_{xy} - ku^1_y \tau^1_{yz})\right] \\ &= -De^{-1}\tau^0_{yy} \end{aligned} \tag{A9}$$

$$\tau^1_{yy,t} + u^1_x \tau^0_{yy,x} - 2\varepsilon[u^1_{y,x}(\tau^s_{xy} + \tau^0_{xy}) + \tau^1_{xy}(u^s_{y,x} + u^1_{y,x})] = -De^{-1}\tau^1_{yy} \tag{A10}$$

$$\tau^0_{zz,t} + \frac{1}{2}(u^1_x \tau^1_{zz,x} - 3ku^1_z \tau^1_{zz}) + \frac{1}{2}u^1_{z,x}\tau^1_{xz} = -De^{-1}\tau^0_{zz} \tag{A11}$$

$$\tau^1_{zz,t} + u^1_x \tau^0_{zz,x} - 2ku^1_z \tau^0_{zz} = -De^{-1}(\tau^1_{zz} + 2aku^1_z) \tag{A12}$$

$$\tau^0_{xy,t} + \frac{u^1_x}{2}(\tau^1_{xy,x} + k\tau^1_{yz}) - \frac{1}{2}(\tau^1_{xx}u^1_{y,x} - ku^1_y \tau^1_{xz}) - u^0_{y,x}\tau^0_{xx} = -De^{-1}(\tau^0_{xy} + au^0_{y,x}) \tag{A13}$$

$$\tau^1_{xy,t} + u^1_x \tau^0_{xy,x} - \tau^1_{xx}(u^s_{y,x} + u^0_{y,x}) - u^1_{x,x}(\tau^s_{xy} + \tau^0_{xy}) = -De^{-1}(\tau^1_{xy} + au^1_{y,x}) \tag{A14}$$

$$\tau^1_{xz,t} - u^1_{z,x}\tau^0_{xx} + ku^1_x \tau^0_{zz} = -De^{-1}\lfloor \tau^1_{xz} + a(u^1_{z,x} - ku^1_x)\rfloor \tag{A15}$$

$$\tau^1_{yz,t} - u^1_{z,x}(\tau^s_{xy} + \tau^0_{xy}) - \tau^1_{xz}(u^s_{y,x} + u^0_{y,x}) + ku^1_y \tau^0_{zz} = -De^{-1}(\tau^1_{yz} - aku^1_y) \tag{A16}$$

So far, no boundary conditions have been imposed other than the assumption of periodicity in the z direction. The stick boundary conditions for Equations (A2)–(A16) become:

$$u^1_x(x = \pm 1/2, t) = u^a_y(x = \pm 1/2, t) = u^1_z(x = \pm 1/2, t) = 0, \quad a = 0, 1 \tag{A17}$$

APPENDIX B: THE 20-DIMENSIONAL DYNAMICAL SYSTEM

The generalization of solution (40) leads to the following expressions for the flow field:

$$u^1_x(x,t) = u^{11}_x(t)\Phi_1(x) + u^{12}_x(t)\Phi_2(x) \tag{B1}$$

$$u_y^a(x,t) = u_y^{a1}(t)\Phi_1(x) + u_y^{a2}(t)\Phi_2(x), \quad a = 0,1 \tag{B2}$$

$$u_z^1(x,t) = u_z^{11}(t)\Phi_1^p(x) + u_z^{12}(t)\Phi_2^p(x) \tag{B3}$$

$$\tau_{ii}^a(x,t) = \tau_{ii}^{a1}(t)\Phi_1^p(x) + \tau_{ii}^{a2}(t)\Phi_2^p(x), \quad i = x,y,z \text{ (no sum)} \tag{B4}$$

$$\tau_{xy}^a(x,t) = \tau_{xy}^{a1}(t)\Phi_1^p(x) + \tau_{xy}^{a2}(t)\Phi_2^p(x), \quad a = 0,1 \tag{B5}$$

$$\tau_{\alpha z}^a(x,t) = \tau_{\alpha z}^{a1}(t)\Phi_1(x) + \tau_{\alpha z}^{a2}(t)\Phi_2(x), \quad \alpha = x,y \tag{B6}$$

$$p^1(x,t) = p_1^1(t)\Phi_1^p(x) + p_2^1(t)\Phi_2^p(x) \tag{B7}$$

where $\Phi_1^p(x)$ and $\Phi_2^p(x)$ are related to the derivatives of the Chandrasekhar functions, and are given in Appendix C.

Upon projection of the two modes in Equations (B1)–(B7) onto Equations (A2)–(A16), and eliminating the pressure coefficient, one obtains a nonlinear dynamical system with 20° of freedom. The system is algebraically involved, and therefore will not be given explicitly here. Compactly, however, the system may be written as

$$\frac{\mathrm{d}x_i}{\mathrm{d}t} = F_i(x_1,\ldots,x_{20}; De), \quad i \in [1,20] \tag{B8}$$

where $x_i(t)$ is a 20-dimensional vector involving the stress coefficients:

$$\begin{aligned} &x_1 = \tau_{xx}^{01}, \quad x_2 = \tau_{xx}^{02}, \quad x_3 = \tau_{xx}^{11}, \quad x_4 = \tau_{xx}^{12} \\ &x_5 = \tau_{yy}^{01}, \quad x_6 = \tau_{yy}^{02}, \quad x_7 = \tau_{yy}^{11}, \quad x_8 = \tau_{yy}^{12} \\ &x_9 = \tau_{zz}^{01}, \quad x_{10} = \tau_{zz}^{02}, \quad x_{11} = \tau_{zz}^{11}, \quad x_{12} = \tau_{zz}^{12} \\ &x_{13} = \tau_{xy}^{01}, \quad x_{14} = \tau_{xy}^{02}, \quad x_{15} = \tau_{xy}^{11}, \quad x_{16} = \tau_{xy}^{12} \\ &x_{17} = \tau_{xz}^{11}, \quad x_{18} = \tau_{xz}^{12}, \quad x_{19} = \tau_{yz}^{11}, \quad x_{20} = \tau_{yz}^{12} \end{aligned} \tag{B9}$$

APPENDIX C: INTEGRALS INVOLVING ORTHOGONAL FUNCTIONS

The various constants in the nonlinear dynamical system (B8) originate from the Galerkin projection of Equations (A2)–(A16) onto modes (B1)–(B7). They are inner products of the form

$$\langle \cdot / \cdot \rangle \equiv \int_{-1/2}^{1/2} \cdot \cdot \, \mathrm{d}x \tag{C1}$$

of Chandrasekhar functions

$$\Phi_1(x) = \frac{\cosh(\lambda x)}{\cosh(\lambda/2)} - \frac{\cos(\lambda x)}{\cos(\lambda/2)}, \quad \Phi_2(x) = \frac{\sinh(\mu x)}{\sinh(\mu/2)} - \frac{\sin(\mu x)}{\sin(\mu/2)} \tag{C2}$$

and quantities related to their derivatives

$$\Phi_1^p(x) = \frac{\sinh(\lambda x)}{\cosh(\lambda/2)} + \frac{\sin(\lambda x)}{\cos(\lambda/2)}, \quad \Phi_2^p(x) = \frac{\cosh(\mu x)}{\sinh(\mu/2)} - \frac{\cos(\mu x)}{\sin(\mu/2)} \tag{C3}$$

$$\Phi_1^{pp}(x) = \frac{\cosh(\lambda x)}{\cosh(\lambda/2)} + \frac{\cos(\lambda x)}{\cos(\lambda/2)}, \quad \Phi_2^{pp}(x) = \frac{\sinh(\mu x)}{\sinh(\mu/2)} + \frac{\sin(\mu x)}{\sin(\mu/2)} \tag{C4}$$

The condition of orthogonality and boundary conditions (A17) lead to the following equations for the constants λ and μ:

$$\tanh(\lambda/2) + \tan(\lambda/2) = \coth(\mu/2) - \cot(\mu/2) = 0 \tag{C5}$$

Thus, the constants are given by:

$$C_1 = \langle \Phi_1^{pp}/\Phi_1 \rangle = -0.5498 \quad C_2 = \langle x\Phi_2/\Phi_1 \rangle = +0.1478$$

$$C_3 = \langle \Phi_2^p/\Phi_1 \rangle = +0.4255 \quad C_4 = \langle \Phi_1^2/\Phi_1 \rangle = +1.3294$$

$$C_5 = \langle \Phi_2^2/\Phi_1 \rangle = 0.9967 \quad C_6 = \langle \Phi_2^{pp}/\Phi_2 \rangle = -0.7467$$

$$C_7 = \langle \Phi_1^p/\Phi_2 \rangle = -0.7065 \quad C_8 = \langle \Phi_2\Phi_1^p/\Phi_1 \rangle = -0.6384$$

$$C_9 = \langle \Phi_1\Phi_2^p/\Phi_1 \rangle = +0.7691 \quad C_{10} = \langle \Phi_2\Phi_1^{pp}/\Phi_1^p \rangle / \langle \Phi_1^p/\Phi_1^p \rangle = +0.2781$$

$$C_{11} = \langle \Phi_2^p\Phi_1^p/\Phi_1^p \rangle / \langle \Phi_1^p/\Phi_1^p \rangle = -0.3349$$

$$C_{12} = \langle \Phi_2^{pp}\Phi_1/\Phi_1^p \rangle / \langle \Phi_1^p/\Phi_1^p \rangle = +0.9839$$

$$C_{13} = \langle \Phi_1^{pp}\Phi_1/\Phi_2^p \rangle / \langle \Phi_2^p/\Phi_2^p \rangle = +0.8953$$

$$C_{14} = \langle \Phi_2^{pp}\Phi_2/\Phi_2^p \rangle / \langle \Phi_2^p/\Phi_2^p \rangle = -0.1819$$

$$C_{15} = \langle \Phi_2^p\Phi_2^p/\Phi_2^p \rangle / \langle \Phi_2^p/\Phi_2^p \rangle = +0.3638$$

$$C_{16} = \langle \Phi_1^2/\Phi_2^p \rangle / \langle \Phi_2^p/\Phi_2^p \rangle = +1.0299$$

$$C_{17} = \langle \Phi_1^p\Phi_1^p/\Phi_2^p \rangle / \langle \Phi_2^p/\Phi_2^p \rangle = -0.2467$$

$$C_{18} = \langle \Phi_1\Phi_2/\Phi_1^p \rangle / \langle \Phi_1^p/\Phi_1^p \rangle = -1.1609$$

$$C_{19} = \langle \Phi_1^{pp}\Phi_2^p/\Phi_1 \rangle / \langle \Phi_1/\Phi_1 \rangle = -0.6385$$

$$C_{20} = \langle \Phi_2^{pp}\Phi_1^p/\Phi_1 \rangle / \langle \Phi_1/\Phi_1 \rangle = +0.5136$$

$$C_{21} = \langle \Phi_1^{pp}\Phi_1^p/\Phi_2 \rangle / \langle \Phi_2/\Phi_2 \rangle = +0.1532$$

$$C_{22} = \langle \Phi_2^{pp}\Phi_2^p/\Phi_2 \rangle / \langle \Phi_2/\Phi_2 \rangle = -0.1358$$

Two additional constants are also introduced, namely

$$\tau_1 = k^2 - \lambda^2 C_1, \quad \tau_2 = k^2 - \mu^2 C_6$$

APPENDIX D: DERIVATION OF THE CHARACTERISTIC EQUATION

The first step in the derivation of the characteristic Equation (43) consists of substituting the velocity and stress coefficients from Equation (42) into system (B8). Upon neglecting the nonlinear terms, one immediately notes the decoupling between $\bar{u}_y^{0i}, \bar{\tau}_{xx}^{0i}, \bar{\tau}_{yy}^{0i}, \bar{\tau}_{zz}^{0i}, \bar{\tau}_{yz}^{0i}$ and the remaining coefficients. Since the former lead to uninteresting transients, they will not be considered any further. The remaining stress coefficients are cast in terms of the velocity components, leading to:

$$\bar{\tau}_{xx}^{11} = -2a\lambda D\bar{u}_x^{11} \tag{D1}$$

$$\bar{\tau}_{xx}^{12} = -2a\lambda D\bar{u}_x^{12} \tag{D2}$$

$$\bar{\tau}_{yy}^{11} = -2a\lambda DDe[DDe(1+2D)\bar{u}_x^{11} - (1+D)\bar{u}_y^{11}] \tag{D3}$$

$$\bar{\tau}_{yy}^{12} = -2a\mu DDe[DDe(1+2D)\bar{u}_x^{12} - (1+D)\bar{u}_y^{12}] \tag{D4}$$

$$\bar{\tau}_{zz}^{11} = +2a\lambda D\bar{u}_x^{11} \tag{D5}$$

$$\bar{\tau}_{zz}^{12} = +2a\lambda D\bar{u}_x^{12} \tag{D6}$$

$$\bar{\tau}_{xy}^{11} = a\lambda D[De(1+2D)\bar{u}_x^{11} - \bar{u}_y^{11}] \tag{D7}$$

$$\bar{\tau}_{xy}^{12} = a\mu D[De(1+2D)\bar{u}_x^{12} - \bar{u}_y^{12}] \tag{D8}$$

$$\bar{\tau}_{xz}^{11} = \frac{aD}{k}(k^2 + C_1\lambda^2)\bar{u}_x^{11} \tag{D9}$$

$$\bar{\tau}_{xz}^{12} = \frac{aD}{k}(k^2 + C_6\mu^2)\bar{u}_x^{12} \tag{D10}$$

$$\bar{\tau}_{yz}^{11} = -\frac{aD}{k}\{De[Dk^2 + (1+D)C_1\lambda^2]\bar{u}_x^{11} - k^2\bar{u}_y^{11}\} \tag{D11}$$

$$\bar{\tau}_{yz}^{12} = -\frac{aD}{k}\{De[Dk^2 + (1+D)C_6\mu^2]\bar{u}_x^{12} - k^2\bar{u}_y^{12}\} \tag{D12}$$

One now seeks the expressions relating the x and y velocity coefficients, which are obtained by substituting for the xy and yz coefficients from (D7), (D8), (D11) and (D12) into Equation (B33). This leads to:

$$\bar{u}_y^{11} = \frac{D^2De}{Rv + D}\bar{u}_x^{11} \tag{D13}$$

$$\bar{u}_y^{12} = \frac{D^2De}{Rv + D}\bar{u}_x^{12} \tag{D14}$$

If Equations (D1)–(D6), (D9) and (D10) are substituted together with (D13) and (D14) into Equations (B29) and (B30), then one obtains the following system for $\bar{u}_x^{11}$ and $\bar{u}_x^{12}$:

$$[Rv(\lambda^4 + k^4 - 2C_1\lambda^2 k^2) + D\tau_1^2]\bar{u}_x^{11} + \frac{2\mu C_3 k^2 D^2 \varepsilon De^2}{Rv + D}[D^2 + Rv(1 + 2D)]\bar{u}_x^{12} = 0 \tag{D15}$$

$$\frac{2\lambda C_7 k^2 D^2 \varepsilon De^2}{Rv + D}[D^2 + Rv(1 + 2D)]\bar{u}_x^{11} + [Rv(\mu^4 + k^4 - 2C_6\mu^2 k^2) + D\tau_2^2]\bar{u}_x^{12} = 0 \tag{D16}$$

For a nontrivial solution, this system leads to the desired characteristic Equation (43).

APPENDIX E: THE AMPLITUDE EQUATION

In this Appendix, the complex coefficients, β_1 and β_2, in the amplitude Equation (49):

$$\frac{\partial A}{\partial T} = \alpha\beta_1 A + 4\beta_2 A^2 A^* \tag{E1}$$

are explicitly given in terms of the Jacobian matrix components, $F_{i,j}$, its right and left eigenvectors, p_i and q_i, and related quantities. Thus, one has [64]

$$\beta_1 = q_i B_{ij} p_j, \quad \beta_2 = 2q_i F_{i,jk}(2p_j r_k + p_j^* s_k) \tag{E2}$$

where B_{ij}, r_i and s_i must satisfy, respectively, the following relations:

$$B_{ij} y_j = F_{i,De}, \quad F_{i,j} r_j = -\frac{1}{2} F_{i,jk} p_j p_k^*, \quad (2i\omega\delta_{ij} - F_{i,j}) s_j = \frac{1}{2} F_{i,jk} p_j p_k \tag{E3}$$

It is clear from system (B8) that since the F_i's are quadratic in the stress coefficients, then the B_{ij}'s are constants; the nonzero components being given by:

$$B_{11} = B_{22} = \frac{1}{De^2}$$

$$B_{33} = \frac{1}{De^2}(1 + 2a\lambda a_3), \quad B_{38} = \frac{2}{De^2} a\lambda a_8, \quad B_{311} = \frac{2}{De^2} a\lambda a_{11}$$

$$B_{317} = \frac{2}{De^2} a\lambda a_{17}$$

$$B_{44} = \frac{1}{De^2}(1 + 2a\mu b_4), \quad B_{47} = \frac{2}{De^2} a\mu b_7, \quad B_{412} = \frac{2}{De^2} a\mu b_{12}$$

$$B_{418} = \frac{2}{De^2} a\mu b_{18}$$

$$B_{55} = B_{66} = B_{77} = B_{88} = B_{99} = B_{1010} = \frac{1}{De^2}$$

$$B_{11\,11} = \frac{1}{De^2}(1 - 2a\lambda a_{11}), \quad B_{11\,3} = -\frac{2}{De^2}a\lambda a_3, \quad B_{11\,8} = -\frac{2}{De^2}a\lambda a_8$$

$$B_{11\,17} = -\frac{2}{De^2}a\lambda a_{17}$$

$$B_{12\,12} = \frac{1}{De^2}(1 - 2a\mu b_{12}), \quad B_{12\,7} = -\frac{2}{De^2}a\mu b_7, \quad B_{12\,4} = -\frac{2}{De^2}a\mu b_4$$

$$B_{12\,18} = -\frac{2}{De^2}a\mu b_{18}$$

$$B_{13\,13} = B_{14\,14} = \frac{1}{De^2}\left(1 + \frac{1}{Rv}\right)$$

$$B_{15\,15} = \frac{1}{De^2}(1 + a\lambda c_{15}), \quad B_{15\,19} = \frac{1}{De^2}a\lambda c_{19}$$

$$B_{16\,16} = \frac{1}{De^2}(1 + a\mu d_{16}), \quad B_{16\,20} = \frac{1}{De^2}a\mu d_{20}$$

$$B_{17\,3} = -\frac{a}{De^2 k}(k^2 + \lambda^2 C_1)a_3, \quad B_{17\,8} = -\frac{a}{De^2 k}(k^2 + \lambda^2 C_1)a_8$$

$$B_{17\,11} = -\frac{a}{De^2 k}(k^2 + \lambda^2 C_1)a_{11}, \quad B_{17\,17} = \frac{1}{De^2}\left[1 - \frac{a}{k}(k^2 + \lambda^2 C_1)a_{17}\right]$$

$$B_{18\,4} = -\frac{a}{De^2 k}(k^2 + \mu^2 C_6)b_4, \quad B_{18\,7} = -\frac{a}{De^2 k}(k^2 + \mu^2 C_6)b_7$$

$$B_{18\,12} = -\frac{a}{De^2 k}(k^2 + \mu^2 C_{61})b_{12}, \quad B_{18\,18} = \frac{1}{De^2}\left[1 - \frac{a}{k}(k^2 + \mu^2 C_6)b_{18}\right]$$

$$B_{19\,15} = -\frac{1}{De^2}akc_{15}, \quad B_{19\,19} = \frac{1}{De^2}(1 - akc_{19})$$

$$B_{20\,16} = -\frac{1}{De^2}akd_{16}, \quad B_{20\,20} = \frac{1}{De^2}(1 - akd_{20})$$

where the following abbreviations were introduced:

$$a_3 = -a_{11} = -\frac{\lambda C_1 k^2}{aRv(\lambda^4 + k^4 - 2\lambda^2 k^2 C_1)}, \quad a_8 = \frac{C_3 k^2}{aRv(\lambda^4 + k^4 - 2\lambda^2 k^2 C_1)}$$

$$a_{17} - \frac{k(\lambda^2 C_1 + k^2)}{aRv(\lambda^4 + k^4 - 2\lambda^2 k^2 C_1)}$$

$$b_4 = -b_{12} = -\frac{\mu C_6 k^2}{aRv(\mu^4 + k^4 - 2\mu^2 k^2 C_6)}, \quad b_7 = \frac{C_7 k^2}{aRv(\mu^4 + k^4 - 2\mu^2 k^2 C_6)}$$

$$b_{18} - \frac{k(\mu^2 C_6 + k^2)}{aRv(\mu^4 + k^4 - 2\mu^2 k^2 C_6)}$$

$$c_{15} - \frac{\lambda C_1}{\tau_1 aRv}, \quad c_{19} - \frac{k}{\tau_1 aRv}$$

$$d_{16} - \frac{\mu C_6}{\tau_2 aRv}, \quad d_{20} - \frac{k}{\tau_2 aRv}$$

ACKNOWLEDGEMENTS

This work is supported by the Natural Sciences and Engineering Research Council of Canada.

REFERENCES

1. Muller SJ, Shaqfeh ESJ, Larson RG. Experimental study of the onset of oscillatory instability in viscoelastic Taylor–Couette flow. *Journal of Non-Newtonian Fluid Mechanics* 1993; **46**:315.
2. Taylor GI. Stability of a viscous liquid contained between two rotating cylinders. *Philosophical Transactions of the Royal Society A* 1923; **223**:289.
3. Benjamin TB. Bifurcation phenomena in steady flow of a viscous fluid. *Proceedings of the Royal Society of London A* 1978; **239**:1.
4. Shaeffer DE. Qualitative analysis of a model for boundary effects in the Taylor problem. *Mathematical Proceedings of the Cambridge Philosophical Society* 1980; **87**:307.
5. Coles D. Transition in circular Couette flow. *Journal of Fluid Mechanics* 1965; **21**:385.
6. Bird RB, Armstrong RC, Hassager O. *Dynamics of Polymeric Liquids*, vol. 1, 2nd edn. John Wiley & Sons: New York, 1987.
7. Larson RG. Instabilities in viscoelastic flows. *Rheological Acta* 1992; **31**:213.
8. Larson RG, Shaqfeh ESG, Muller SJ. A purely elastic instability in Taylor–Couette flow. *Journal of Fluid Mechanics* 1990; **218**:573.
9. Shaqfeh ESG, Muller SJ, Larson RG. The effect of gap width and dilute solution properties on the viscoelastic Taylor–Couette instabilities. *Journal of Fluid Mechanics* 1992; **235**:285.
10. Chossat P, Iooss G. *The Couette–Taylor Problem*. Springer-Verlag: New York, 1991.
11. Sell GR, Foias C, Temam R. *Turbulence in Fluid Flows: A dynamical systems Approach*. Springer-Verlag: New York, 1993.
12. Holmes P, Lumley JL, Berkooz G. *Turbulence*, *Coherent Structures*, *Dynamical Systems and Symmetry*. Cambridge University Press: Cambridge, 1996.
13. Lorenz EN. Deterministic nonperiodic flow. *Journal of Atmospheric Science* 1963; **20**:130.
14. Shirer HN, Wells R. *Mathematical Structure of the Singularities at the Transition Between Steady States in Hydrodynamic Systems*. Springer-Verlag: Heidelberg, 1980.
15. Veronis G. Motions at subcritical values of the Rayleigh number in a rotating fluid. *Journal of Fluid Mechanics* 1996; **24**:545.
16. McLaughlin JB, Martin PC. Transition to turbulence in a statically stressed fluid system. *Physics Review A* 1975; **12**:186.
17. Curry JH. A generalized Lorenz system. *Communications in Mathematical Physics* 1978; **60**:193.
18. Yorke JA, Yorke ED. *Hydrodynamic Instabilities and the Transition to Turbulence* Swinney HL, Gollub JP (eds). Springer-Verlag: Berlin, 1981.
19. Pomeau Y, Manneville P. Intermittent transition to turbulence in dissipative systems. *Communications in Mathematical Physics* 1980; **74**:189.
20. Sparrow C. *The Lorenz Equations.* Springer-Verlag: New York, 1983.
21. Yahata H. Temporal development of the Taylor vortices in a rotating field. 1, *Programmes in Theoretical Physics* 1979; **61**:791.
22. Yahata H. Temporal development of the Taylor vortices in a rotating field. 2, *Programmes in Theoretical Physics* 1979; **61**:791.
23. Kuhlmann H. Model for Taylor–Couette Flow. *Physics Review A* 1985; **32**:1703.
24. Kuhlmann H, Roth D, Luke M. Taylor flow and harmonic modulation of the deriving force. *Physics Review A* 1988; **39**:745.
25. Fenstermacher PR, Swinney HL, Gollub JP. Dynamical instabilities and the transition to chaotic Taylor vortex flow. *Journal of Fluid Mechanics* 1979; **94**:103.
26. Gorman M, Swinney HL. Spatial and temporal characteristics of modulated waves in the circular Couette system. *Journal of Fluid Mechanics* 1982; **117**:123.

27. Deane AE, Keverkidis IG, Karniakadis GE, Orszag SA. Low-dimensional models for complex flows: Application to grooved channels and circular cylinders. *Physics of Fluids A* 1991; **3**:2337.
28. Stone E. A Study of Low-Dimensional Models for the Wall Region of a Turbulent Layer. PhD thesis. Cornell University, 1989.
29. Zheng X, Glauser MN, A low-dimensional description of the axisymmetric jet mixing layer. *ASME Computers in Engineering* 1990; **2**:211.
30. Rosenblatt J. Thermal convection in a viscoelastic fluid. *Journal of Non-Newtonian Fluid Mechanics* 1986; **21**:201.
31. Khayat RE. Chaos and overstability in the thermal convection of viscoelastic fluids. *Journal of Non-Newtonian Fluid Mechanics* 1994; **5**:227.
32. Khayat RE. Nonlinear overstability in the thermal convection of viscoelastic fluids. *Journal of Non-Newtonian Fluid Mechanics* 1995; **58**:331.
33. Khayat RE. Fluid elasticity and transition to chaos in thermal convection. *Physics Review E* 1995; **51**:380.
34. Khayat RE. Onset of chaos in the thermal convection of weakly shear thinning fluids. *Journal of Non-Newtonian Fluid Mechanics* 1996; **63**:153.
35. Khayat RE. Onset of Taylor vortices and chaos in viscoelastic fluids. *Physics of Fluids A* 1995; **7**:2191.
36. Khayat RE. Low-dimensional approach to nonlinear overstability of purely elastic Taylor-vortex flow. *Physics Review Letters* 1997; **78**:4918.
37. Ashrafi N, Khayat RE. Shear-thinning induced chaos in Taylor–Couette flow. *Physics Review E*, in press.
38. Ashrafi N, Khayat RE. A low-dimensional approach to nonlinear plane-Couette flow of viscoelastic fluids. *Physics of Fluids*, in press.
39. Avgousti M, Beris AN. Non-axisymmetric modes in viscoelastic Taylor–Couette flow. *Journal of Non-Newtonian Fluid Mechanics* 1993; **53**:225.
40. Northey PJ, Armstrong RC, Brown RA. Finite-amplitude time-periodic states in viscoelastic Taylor–Couette flow described by the UCM model. *Journal of Non-Newtonian Fluid Mechanics* 1992; **42**:117.
41. Avgousti M, Liu M, Beris AN. Spectral methods for the viscoelastic time-dependent flow equations with applications to Taylor–Couette flow. *International Journal of Numerical Methods in Fluids* 1993; **17**:49.
42. Sureshkumar R, Beris AN, Avgousti M. Non-axisymmetric subcritical bifurcations in viscoelastic Taylor–Couette flow. *Proceedings of the Royal Society of London A* 1994; **447**:135.
43. Shaqfeh ESG. Purely elastic instabilities in viscoelastic flows. *Annual Review of Fluid Mechanics* 1996; **28**:129.
44. Groisman A, Steinberg V. Couette–Taylor flow in a dilute polymer solution. *Physics Review Letters* 1996; **77**:1480.
45. Groisman A, Steinberg V. Solitary vortex pairs in viscoelastic Couette flow *Physics Review Letters* 1997; **78**:1460.
46. Larson RG. Taylor–Couette stability analysis for a Doi-Edwards fluid. *Rheological Acta* 1989; **28**:504.
47. Larson RG, Muller SJ, Shaqfeh ESG. The effect of fluid rheology on the elastic Taylor–Couette instability. *Journal of Non-Newtonian Fluid Mechanics* 1994; **51**:195.
48. Guckenheimer J, Holmes P. *Nonlinear Oscillations*, *Dynamical Systems*, *and Bifurcations of Vector Fields*. Springer-Verlag: New York, 1983.
49. Ott E. *Chaos in Dynamical Systems*. University Press: Cambridge, 1993.
50. Boger DV. A highly elastic constant-viscosity fluid. *Journal of Non-Newtonian Fluid Mechanics* 1977/1978; **3**:87.
51. Mackay ME, Boger DV. An explanation of the rheological properties of Boger fluids. *Journal of Non-Newtonian Fluid Mechanics* 1987; **22**:235.
52. Kentock M, Georgescu AG, Sherwood AA, Tanner RI. The measurement of the second normal stress difference for some polymer solution. *Journal of Non-Newtonian Fluid Mechanics* 1980; **6**:303.
53. Nagata M. Bifurcation in Couette flow between almost corotating cylinders. *Journal of Fluid Mechanics* 1986; **169**:229.
54. Tabeling P. Dynamic of the phase variable in the Taylor vortex system. *Journal of Physics Letters* 1983; **44**:665.
55. Richtmyer RD. A method for the calculation of invariant manifolds in hydrodynamic instability problems. TN-176+STR, 1981.
56. Marcus PS. Simulation of Taylor–Couette flow. Part 2. Numerical results for wavy-vortex flow with one travelling wave. *Journal of Fluid Mechanics* 1984; **146**:65.
57. Chandrasekhar S. *Hydrodynamic and Hydromagnetic Stability*. Dover: New York, 1961.
58. Grosch CE, Harold S. The stability of steady and time-dependent plane Poiseuille flow. *Journal of Fluid Mechanics* 1968; **34**:177.
59. Drazin PG, Reid WH. *Hydrodynamic Stability.* Cambridge University Press: Cambridge, 1981.
60. Baumert BM, Muller S. Flow visualization of the elastic Taylor–Couette flow in Boger fluids. *Rheological Acta* 1995; **34**:147.
61. Baumert BM, Muller S. Axisymmetric and non-axisymmetric elastic and inertio-elastic instabilities in Taylor–Couette flow. *Journal of Non-Newtonian Fluid Mechanics* 1999; **83**:33.

62. Carr J. *Applications of the Center Manifold Theory*. Springer-Verlag: New York, 1981.
63. Wiggins S. *Introduction to Applied Nonlinear Dynamical Systems and Chaos*. Springer-Verlag: New York, 1990.
64. Nayfeh AH, Balachadran B. *Applied Nonlinear Dynamics*. John Wiley & Sons: New York, 1995.
65. Nayfeh AH. *Introduction to Perturbation Techniques*. John Wiley and Sons: New York, 1981.
66. Walters K. *Rheometry*: *Industrial Applications*. Research Studies Press, 1980.
67. Tanner RI. *Engineering Rheology*. Oxford University Press: Oxford, 1983.
68. Doi M, Edwards SF. *The Theory of Polymer Dynamics*. Oxford University Press: Oxford, 1988.
69. Eu BC, Khayat RE. Extended irreversible thermodynamics, generalized hydrodynamics, kinetic theory and rheology. *Rheological Acta* 1991; **30**:204.
70. Bird RB, Curtis CF, Armstrong RC, Hassager O. *Dynamics of Polymeric Liquids*, vol. 2, 2nd edn. Wiley: New York, 1987.